Forsmark et al. Integrating Materials and Manufacturing Innovation (2015) 4:6
DOI 10.1186/s40192-015-0033-0

Integrating Materials and Manufacturing Innovation
a SpringerOpen Journal

RESEARCH ARTICLE Open Access

Using quality mapping to predict spatial variation in local properties and component performance in Mg alloy thin-walled high-pressure die castings: an ICME approach and case study

Joy H Forsmark[1*], Jacob W Zindel[1], Larry Godlewski[1], Jiang Zheng[2], John E Allison[2] and Mei Li[1]

* Correspondence: jforsma5@ford.com
[1]Materials Research Department, Ford Motor Company, Research and Innovation Center, MD3182, P.O Box 2053, Dearborn, MI 48121, USA
Full list of author information is available at the end of the article

Abstract

This paper explores the use of quality mapping for the prediction of the spatial variation in local properties in thin-walled high-pressure die castings (HPDC) of the magnesium alloy AM60. The work investigates the role of casting parameters on local ductility and yield strength and presents a model for predicting local ductility and yield strength in a cast component. A design of experiment (DOE) was created to examine the role of various casting parameters on local properties such as ductility and yield strength. Over 1,200 tensile samples were excised from cast parts and tested. Casting simulations were also conducted for each experimental condition. Local properties were predicted, and the local property (quality map) model was compared with a prototype production component. The results of this model were used as input to a performance simulation software code to simulate the component-level behavior under two different loading conditions. In this study, the authors bypassed the traditional Integrated Computational Materials Engineering (ICME; process-microstructure-properties) approach in favor of a semi-empirical quality mapping approach to provide estimates of manufacturing sensitive local properties for use in process and component design.

Keywords: ICME; Magnesium alloys; High-pressure die casting; Casting simulation

Background

As the need for weight savings and fuel economy has increased, so has the interest in using magnesium alloys for a wider variety of automotive applications [1-3]. The low density and favorable stiffness-to-weight ratio of Mg alloys enable considerable weight savings on components. Additionally, the excellent high-pressure die castability of many Mg alloys allows for more complex and one-piece designs compared to traditional steel stampings and even some Al castings. This enables part consolidation and potential cost savings [1]. Thus, most magnesium components are produced by high-pressure die casting (HPDC). However, HPDC Mg alloys do have a lower ductility (elongation at failure) than more commonly used wrought steel or aluminum components. In several studies of the magnesium alloys AM50 and AM60 [4,5], elongation at failure or ductility has been reported to correlate with fracture toughness in Mg alloys.

In general, higher ductility corresponds to better fracture toughness; this is a key concern in the prediction of crash response and optimal design of structures.

Castings, probably to a greater extent than wrought products, exhibit geometry and manufacturing-history-dependent spatial variation in some properties. These geometry and manufacturing-history-dependent spatial variations, also known as location-specific or local properties, should be accounted for in the design of structural applications. Studies of excised tensile samples from production instrument panel components in AM60 have shown that spatial variation in ductility can range from 1% to 14% depending on location within the component [6-9]. A key conclusion from these studies is that an understanding of the spatial variability in the mechanical properties from quasi-static tests is important because the values of ductility in a given location may influence dynamic performance of the component in service [10]. To complicate the situation further, a given property at a given location varies from casting to casting, resulting in another factor to address. One way to look at the situation is that the mean value of a given property is location dependent and each location may have its own statistical variation. Computer-aided engineering (CAE) methods used in design, however, rely on a single material model for all regions of the component to predict the component behavior without taking into account location-specific properties or their distribution about the mean. Therefore, the ability to predict spatial variation in local properties can still lead to improved accuracy in the prediction of the overall behavior of a component and thus increased confidence in and utilization of HPDC Mg components.

In a casting, the measured variation in mechanical properties (both spatial variation within a casting and statistical variation observed at a particular location across multiple castings produced under the same conditions) obtained from excised test samples can be due to several sources:

(1) Variation associated with normal foundry processing conditions (such as melt temperature or local die temperature)
(2) Variation associated with local geometry (such as melt flow paths or section thicknesses)
(3) Variation associated with the location and morphology of microstructural features (such as void size, void percentage, or phase segregation): some variation can be linked to (1) and (2) and some due to randomness of the microstructure formation
(4) Variation associated with testing (such as sample dimensions or loading forces)

A traditional Integrated Computational Materials Engineering (ICME) approach predicts variation in properties due to manufacturing history by directly linking the pertinent local microstructure to the mechanical properties of interest, such as those described by Li et al. [11] and Horstemeyer et al. [12]. Indeed, a number of researchers have investigated the influence of such microstructural features as dendrite arm spacing, externally solidified grain size, shrinkage porosity and oxide films, or cold shuts on the mechanical properties of Mg alloys [7-9,13-34]. However, there still exists a substantial amount of disagreement with regard to the level of influence that particular microstructural features have on this behavior in Mg castings, particularly with regard to local ductility. Further, models to predict the formation of many of these microstructural features are not currently available.

There has been some effort to correlate Mg alloy mechanical properties directly to variations in HPDC processing parameters [26,35-37]. Sannes et al. [26], for example, demonstrated that changing the gating configuration of a tensile bar die produced as-cast tensile specimens that had statistically significant differences in ductility. They also utilized casting simulation to qualitatively show those differences in flow characteristics. There are several commercial casting simulation codes available that can predict the filling and solidification process for a given casting and processing condition. These codes can capture variations in melt flow, air entrapment, and general solidification gradients due to processing conditions and visually map these differences onto a computer model of the part. While some of these codes have limited capability to predict certain microstructural features (e.g., macroporosity caused by unfavorable solidification gradients in certain locations and the occurrence of 'hot spots' in a casting), the capability required to predict the location and size of very fine microstructural features such as microporosity in thin-walled HPDC castings is generally not robust.

In this study, the authors bypassed the traditional ICME (process-microstructure-properties) approach in favor of a semi-empirical quality mapping approach to provide estimates of manufacturing sensitive local properties for use in process and component design. The term 'quality map' describes an empirically derived surrogate model that can be used to predict a particular property using local flow and solidification characteristics in a cast part. The equation itself is then 'mapped' onto the original cast component. In this way, the local properties can be visualized on a cast part and used in a component and engineering system performance simulation. This approach is, by its nature, a less desirable method than the development of a well-correlated model based upon physical principles. However, given that such a physical principle-based model does not exist, the development of a surrogate model using a design space approximation approach is a valid technique for understanding mechanical property behavior in HPDC castings. Other researchers have used the quality mapping approach to predict overall performance in Mg die castings. Greve et al. [38] developed a local casting quality criterion based on the flow conditions and the cooling rate in different regions in an AZ91 clutch housing. Sannes et al. [39], who first used the term 'quality map,' used a U-shaped AM60 casting with a nominal wall thickness of 2 mm in their investigation. They determined the flow and solidification characteristics in the casting which they correlated to a fracture criteria based on observed microstructure. The fracture criteria function was then used in a companion work by Dorum et al. [40-44] to predict the component behavior in quasi-static bending experiments. Weiss et al. [45] also describe a similar quality mapping approach in a study on a box structure in AM50.

The above studies all examined smaller components with box-like or bracket configurations. However, many of the Mg castings used in automotive structural applications have a frame-like geometry. For example, the Corvette engine cradle [46] and the Ford F150 grill opening radiator support [47] both have large frame-like structures. Likewise, closures such as the Aston Martin DB9 door inner [48] and, recently, the rear liftgate inner of the Ford MKT [49] are structures with window openings and have large, long sections. These frame-like structures tend to have some unique features such as the melt flow lengths that exceed 2 to 3 m and areas where melt fronts meet inside the casting.

This project was undertaken to develop a methodology to directly predict location-specific ductility and yield strength in a frame-geometry Mg HPDC casting from the outputs of a commercial casting simulation code and then use those predictions to modify the material input deck of a commercial finite element deformation simulation code to ultimately predict component performance. Figure 1 shows a flow chart of the process. The ultimate goal was to provide an industrially feasible workflow that would allow for component design iterations that takes into account manufacturing history in performance predictions prior to tooling being produced and prototypes manufactured, thus reducing design iterations for a cast component.

Methods and results

Casting of experimental components

Since production parts are complex geometries often with curvature or small changes in section thickness, they are not ideal to determine mechanical properties through excising standard test specimens. Therefore, an experimental casting called the Generic Frame Casting (GFC) was designed to contain features that would be present in a production door inner or other frame casting while still providing sufficient material to produce sub-size tensile samples and allow for ease of fixturing for component-level testing. The part is also closer in size to frame-like castings that are in production. Figure 2 shows a schematic diagram of the as-cast and machined GFC. The GFC has one large window and three smaller windows. There are two symmetrical rib sections along the sides. The GFC outer dimensions are 580 mm × 580 mm, with a 2.5-mm nominal wall thickness over the entire part. The side walls are approximately 50 mm high with a draft angle of approximately 10° for ease of casting. In the GFC, a simple, single gate is attached to the lower wall of the upper aperture and metal enters through this location. Overflows for the metal were cut at the top wall of the upper aperture and the walls of the lower apertures. Gates to the overflows could be cut or welded up, depending on the needs for a particular casting trial. The diagram also indicates the presence of a center feeder which was also used to change the metal flow pattern.

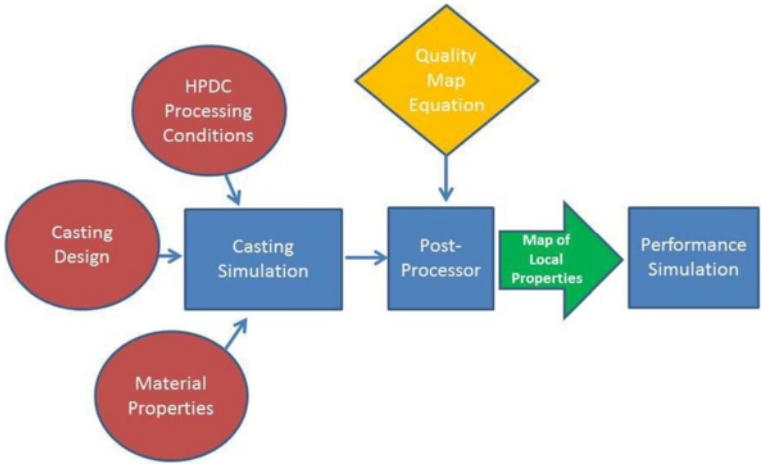

Figure 1 Flow chart of quality mapping process.

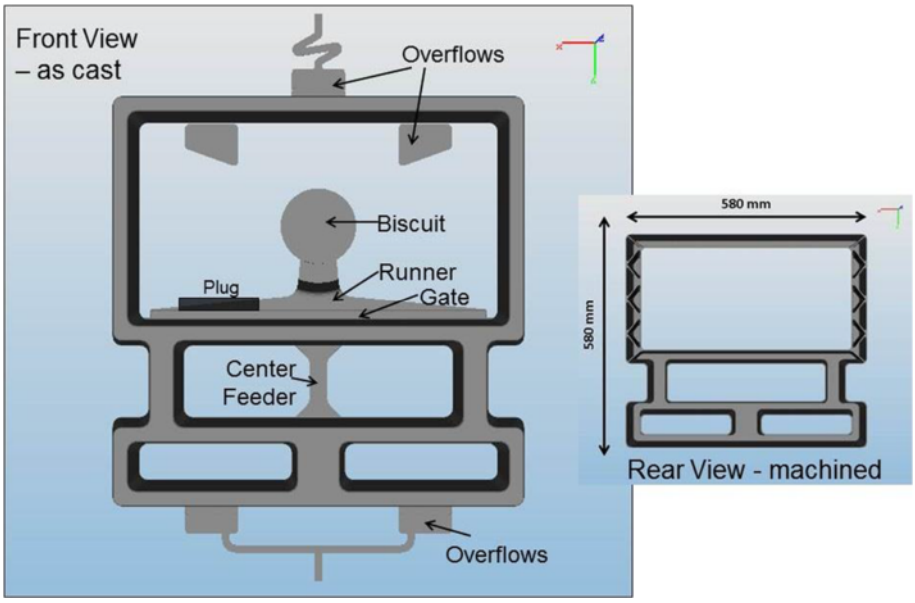

Figure 2 Schematic diagram of the as-cast (front view) and machined (rear view) Generic Frame Casting (GFC).

The gating and overflows were designed using the North American Die Casting Association (NADCA) guidelines for proper gating and casting design to optimize the quality of Mg and other castings [50,51]. They were also confirmed using a MAGMASOFT® simulation prior to the die being produced.

The GFC castings were produced by the authors at Mag-Tec Casting Corporation in Jackson, MI, USA. The parts were cast on a Model 836 Prince/Buehler cold-chamber die casting machine (BuhlerPrince, Inc., Holland, MI, USA) with a molten metal pumping system from the covered furnace. Molten Mg in a furnace must be held under a cover gas to prevent oxidation (SF_6 was used in this case). A schematic diagram of a typical cold-chamber high-pressure die cast machine is shown in Additional file 1. During casting, a specific amount of molten metal is pumped into the shot sleeve from a holding furnace. Pressure is rapidly applied to a plunger which travels the length of the shot sleeve and pushes the metal into the casting cavity in the steel die, where it is held until the metal solidifies and the die then opens, ejecting the part. The actual filling of a typical die cavity takes 20 to 40 ms, and the metal completely solidifies in less than 1 to 2 min with some surface regions solidifying within seconds.

The motion of the plunger as it fills the casting cavity can be visualized by examining the shot profile. In general, the shot profile is represented by a plot of plunger velocity as a function of distance and is divided into three steps: slow shot, transition, and fast shot. The fast shot speed controls the speed of the melt fill of the casting cavity and thus can influence the casting quality. An example of one of the shot profiles from this study can be seen in Figure 3.

Thermocouples placed in the die and furnace indicated the temperature of the melt at the beginning of the production cycle and the casting cavity throughout the production cycle of a cast part. Figure 4 shows the thermal behavior in different areas of the die and furnace during the course of a casting run to produce the component

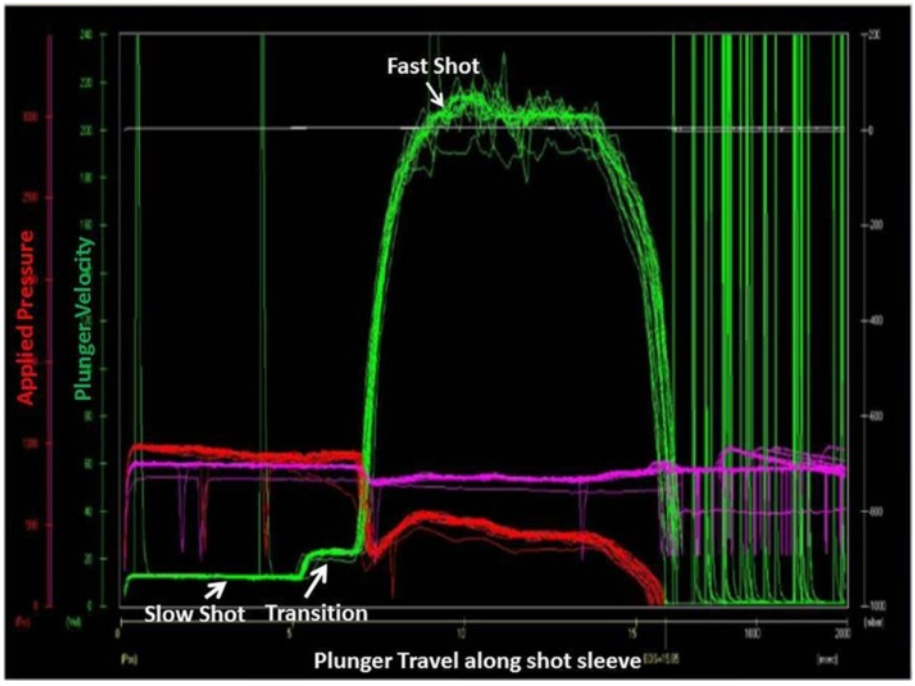

Figure 3 Typical shot profile. The green line indicates the velocity of plunger versus the position in the shot sleeve, and red and magenta lines indicate the pressure applied to the plunger by the machine.

investigated in this study. The figure indicates that the die temperature increased from the initial casting run and achieved a nominal steady state after about eight castings are produced. In many foundry practices, the first few parts cast are discarded as scrap because the die is considered too cold at this point in the trial. Cooling and heating lines were placed in the die to mitigate the thermal variation in the die or enhance a desired thermal gradient in certain locations such as near the biscuit region. The die

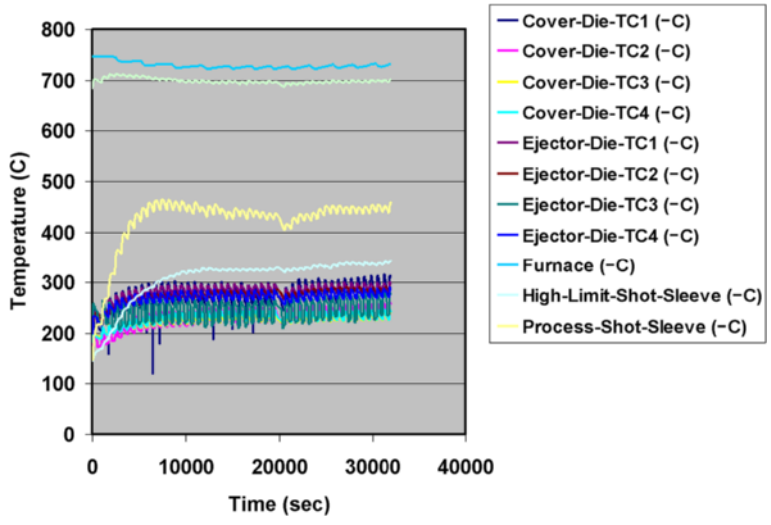

Figure 4 Typical temperature profile in different areas of typical HPDC component, shot sleeve, and furnace during casting trial. Temperature was measured by imbedded thermocouples.

temperature was partially controlled by oil lines cut into the die and run at a temperature of 240°C. Detailed processing conditions were documented for all castings.

A preliminary casting trial was run with the die to determine a process operating window for the GFC casting with the target of producing a complete cast part. Based on the results of the trial, a four-factor, two-level full factorial design of experiment (DOE) was established in order to produce testable components under a range of casting parameters within that window. A total of 16 different sets of castings were produced. The DOE approach was also used because the casting parameters (DOE factors) examined could have confounding effects on the local behavior and it was important to understand the relative weighting of each factor. Two of the casting parameters investigated were processing parameters: fast shot speed and melt temperature. The other two factors were geometrical parameters where the center feeder and a gate plug were either present or not present (see Figure 2). The plug in the gate produced an asymmetrical gating configuration that changed the flow in the part. The symmetrical gating system had a gate area of 9.7 cm^2, while the gate plug reduced the area of the gate down to 7.7 cm^2, in addition to changing the gating flow pattern. Table 1 shows the full factorial DOE with the upper and lower values for each factor.

The alloy composition was carefully controlled for all cases. Table 2 indicates the chemical composition and a comparison with the specification for AM60B. As can be seen in the table, the chemical composition of the alloy contains aluminum content at the lower end of the specification but still considered typical for production components.

In general, 15 castings were produced as die 'warm-up' shots to get the die to a quasi-steady-state temperature as determined by the embedded thermocouples. On average, the 40 to 50 castings that were subsequently produced were used for analysis. If during the course of a casting run, the machine had to be stopped for an extended

Table 1 DOE factors for GFC castings

Condition assignment	Fast shot (m/s)	Melt temperature (°C)	Gating design	Center feeder	Excised sample testing?
A	5.3	660	Symmetrical	No	Yes
B	6.6	660	Symmetrical	No	
C	5.3	700	Symmetrical	No	
D	6.6	700	Symmetrical	No	Yes
E	5.3	660	Asymmetrical	No	
F	6.6	660	Asymmetrical	No	Yes
G	5.3	700	Asymmetrical	No	Yes
H	6.6	700	Asymmetrical	No	
I	5.3	660	Symmetrical	Yes	Yes
J	6.6	660	Symmetrical	Yes	Yes
K	5.3	700	Symmetrical	Yes	Yes
L	6.6	700	Symmetrical	Yes	
M	5.3	660	Asymmetrical	Yes	Yes
N	6.6	660	Asymmetrical	Yes	
P	5.3	700	Asymmetrical	Yes	
Q	6.6	700	Asymmetrical	Yes	Yes

Table 2 Chemical composition of AM60B used in the study

	Al wt%	Zn wt%	Mn wt%	Si wt%	Fe wt%	Cu wt%
AM60	5.7	0.06	0.4	0.01	0.005	0.003
AM60B ASTM B94-07 specification	5.6 to 6.5	0.22	0.24 to 0.6	0.10	<0.005	<0.010

period of time, a small number of 'warm-up' shots would be produced and scrapped until the die returned to steady state before useable castings were made. Over 600 castings were produced during this study.

Excised tensile bar testing

After the castings were produced, tensile samples were excised from eight different locations in up to 20 castings per condition (Figure 5). A total of 8 of the 16 casting runs were selected for evaluation based on the partial factorial DOE (represented by an $L_8(2^{4-1})$ orthogonal array [52]). This experimental design was selected because it allowed for determination of the main effects while still keeping the total number of tensile tests and statistically significant number of replicates manageable; still, a total of 1,280 tensile tests were conducted to complete the experiment. As shown in Table 3, the eight conditions selected for analysis were conditions A, D, J, K, F, G, M, and Q.

The tensile sample geometry was the ASTM E8 standard [53] for sub-sized flat tensile bars with a total length of 76 mm, a gage section of 25.4 mm, and a nominal thickness of 2.5 mm. The edges of the flat, dog-bone-shaped samples were machined using a milling process that resulted in a machined surface roughness of 0.8 μm. The

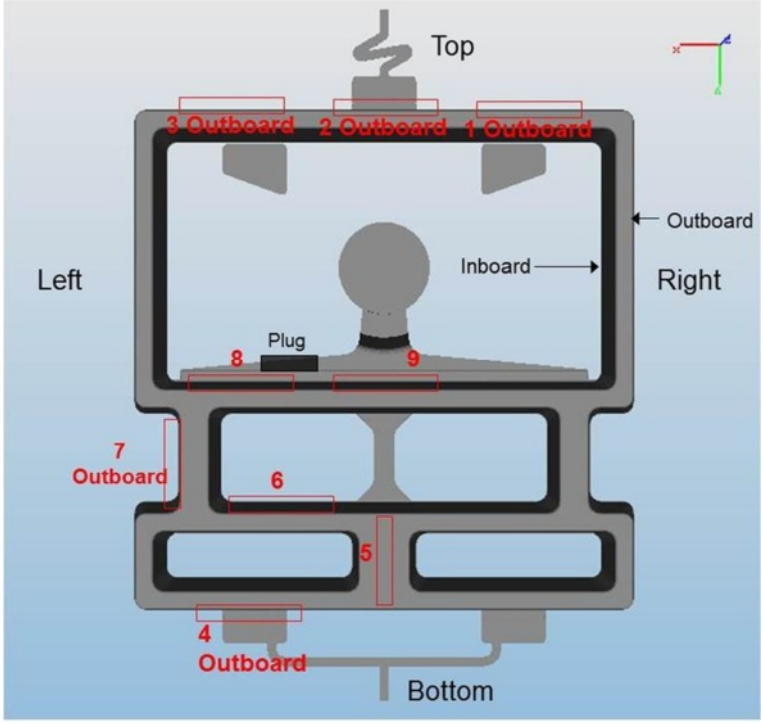

Figure 5 Locations of excised samples in the GFC. Location 9 was only tested in condition U, and outboard refers to the outer wall of the casting.

Table 3 Actual values recorded for processing conditions used for MAGMASOFT simulations

Designation	Alloy	Fast shot (m/s)	Melt temperature (°C)	Gating configuration	Center feeder
A	AM60	5.2	675	No plug	No
J	AM60	6.5	691	No plug	Yes
K	AM60	5.3	711	No plug	Yes
D	AM60	6.6	738	No plug	No
M	AM60	5.2	677	Plug	Yes
F	AM60	6.1	687	Plug	No
G	AM60	5.1	731	Plug	No
Q	AM60	6.1	727	Plug	Yes
U	AM60	5.8	720	Plug	Yes
I	AM60	5.1	685	No plug	Yes

faces of the tensile samples were as-cast (not machined). Tensile samples were tested in axial loading using a Sintech™ frame (MTS Systems Corp., Eden Prairie, MN, USA) with a 133-kN (30,000 lb) load cell and a 25.4-mm gage length extensometer. The frame was operated at a constant crosshead speed of 0.04 mm/s up to 1% strain and then transitioned to a constant cross-head speed of 0.21 mm/s thereafter. This corresponds approximately to strain rates of 1.5×10^{-3} s^{-1} and 8×10^{-3} s^{-1}, respectively.

The load and extensometer data were recorded, and the data was analyzed to give true stress and true strain tensile behavior. The total elongation at failure, also known as tensile ductility, was determined using the final extensometer measurement at failure without removing the elastic strain and was reported as 'elongation at failure' in true strain. Minimal sample necking was observed. Any sample that failed outside the extensometer gage length was removed from the study. Samples that failed prior to reaching yield but within the extensometer gage length were considered for inclusion in the elongation at failure but not for the yield strength or ultimate tensile strength values. Results from a total of 936 tensile samples were reported and used for subsequent analysis.

Statistical (cumulative probability) analysis was conducted at all sample locations indicating that most of the data was distributed normally (Figure 6 shows an example for condition A where p values > 0.05). Because of the normal distribution, average values of both elongation at failure and 0.2% offset yield strength were used in the subsequent analysis to develop the quality mapping relationships. Average values of elongation at failure and 0.2% offset yield strength as a function of location and condition are shown in Figures 7 and 8. To separate the effects of the casting parameters on the locations in the casting, main effects plots were constructed and are shown in Figure 9 for several locations. A main effects plot indicates differences in the responses to different levels used in the input factors in a DOE. If a main effect is not present, the plots indicate a horizontal line. However, if a factor does have an influence on the response (in this case the ductility), the steepness of the line indicates the magnitude of the effect of the factor on the response. For example, Figure 9 shows that gating design had a significant influence on the elongation at failure in all cases. However, the shot speed and melt temperature also had a minor influence on the ductility in locations 2 and 3, while the presence of the center feeder was a factor only for locations 4 and 5.

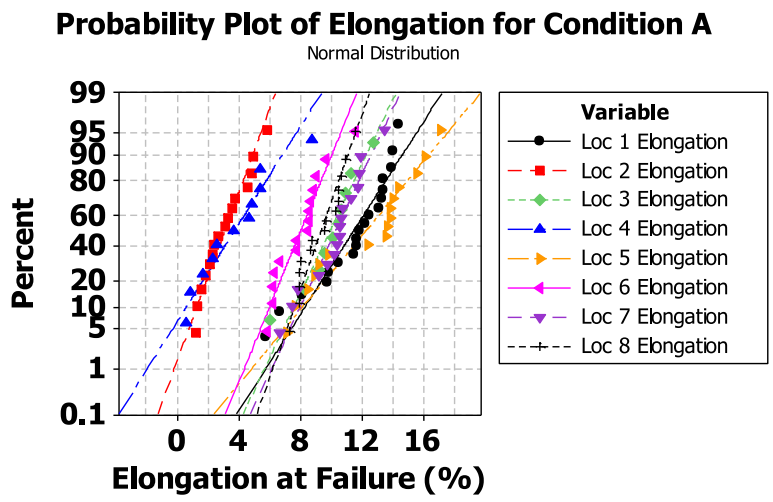

Figure 6 Typical probability plot of %elongation at failure for condition A. A straight line indicates a normal distribution of the data. The data in this sample shows that the total elongation-at-failure measurements were normally distributed.

For the DOE, care was taken to ensure that all other processing parameters outside the four factors being tested remained constant. One important parameter that remained the same throughout the DOE was the location of the overflows. Overflow position is normally optimized to account for geometry and melt flow changes in commercial production. Overflows are generally positioned in areas where melt fronts meet in order to remove defects that could result in those regions from the body of the casting. However, during processing of the DOE castings, the overflows for the asymmetrical gating configuration remained constant and thus were not optimally placed. Upon completion of the DOE experiment, the geometry of the overflows and their locations were modified for the asymmetrical gating geometry factor creating condition U. Condition U had similar processing parameters as condition Q. Figure 10 shows the differences in overflow location for the two castings. Excised sample testing indicated that overflow position did indeed make a difference in the measured ductility in several

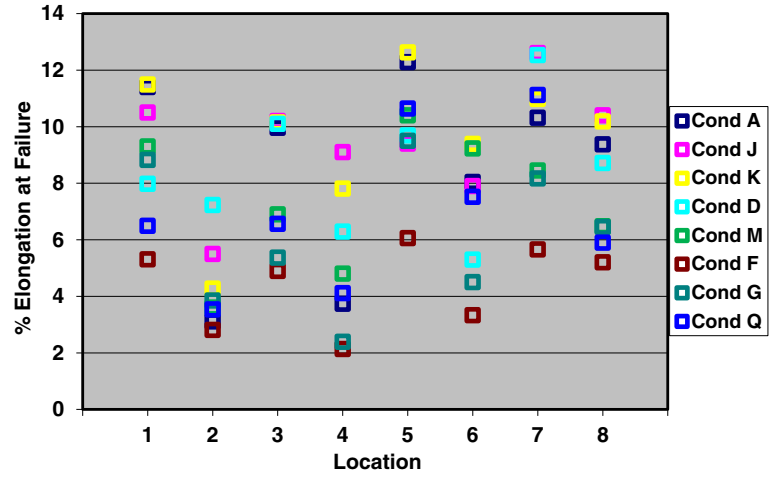

Figure 7 Average values for elongation at failure (%) as a function of location for eight different casting conditions.

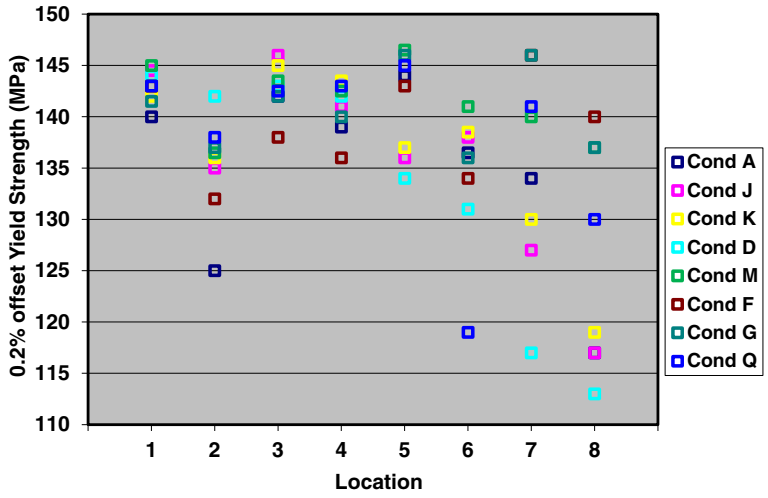

Figure 8 Average values for yield strength (0.2% offset) as a function of location for eight different casting conditions.

locations in the casting (Figure 11). Location 2, in particular, showed significant improvement in average elongation at failure.

With the process window defined, two casting conditions were selected for further study and for use in component-level experiments: condition I and condition U. An additional excised tensile bar location was also identified and tested (location 9, see Figure 5). Figure 12a,b, shows 'box and whisker plots' of the tensile results (elongation, 0.2% offset yield strength, and ultimate tensile strength, respectively) in each of the locations tested for the condition U that were generated in Minitab® version 15. 'Box and whisker' plots present the data in a consistent statistical format by dividing the entire data set into four quartiles [54]. In Minitab®, the top line of the box represents the third quartile of the data set (i.e., 75% of the data are less than or equal to that value). The middle line of the box is the median of the entire data set, and the bottom line of the box represents the first quartile of the data set (i.e., 25% of the data are less than or equal to that value). The vertical lines (whiskers) extend to the maximum data points

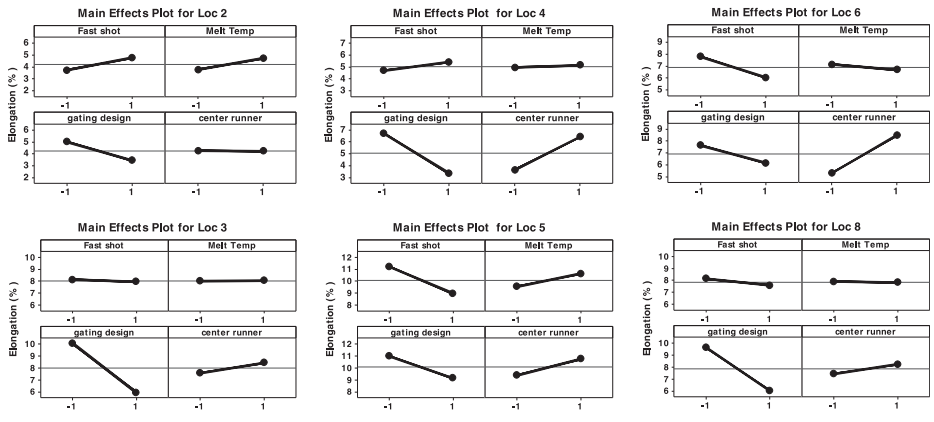

Figure 9 Main effects plots. The figure shows main effects plots for variations in mean elongation at failure (%) versus processing conditions for locations 2, 3, 4, 5, 6 and 8. Note: −1 and +1 represent the extremes of design variables. A horizontal main effects line represents minimal influence.

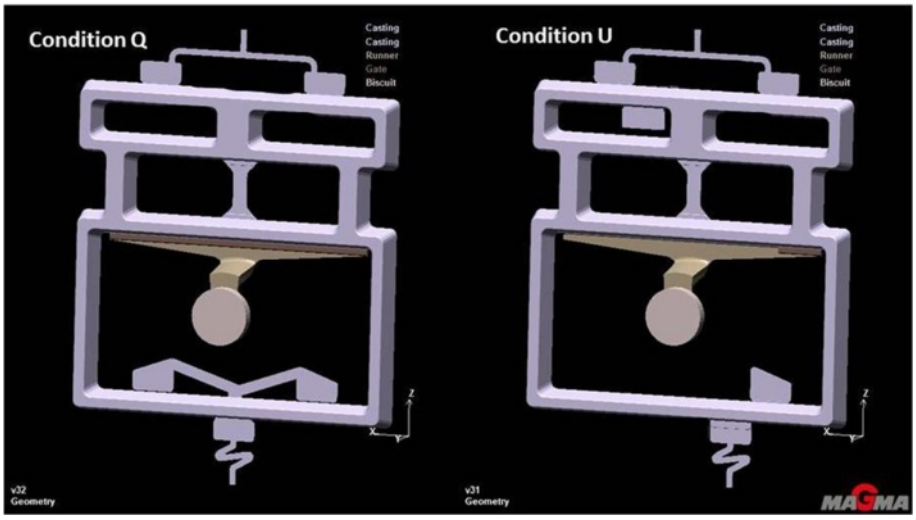

Figure 10 Differences in overflow locations between condition U and condition Q.

in the set that are within 1.5 times the third quartile number and the minimum data points in the set that are within 1.5 times the first quartile number. Stars represent data that lie outside that range [55]. The average elongation at failure for all the samples tested in condition U was 0.08 ± 0.02. An analysis of variation (ANOVA) of the means at each location gave a p value of <0.05, indicating that there was a statistically significant difference in the total elongation at failure in the different locations.

Figure 13 shows the true stress versus true strain curves for a representative sample; in this case, location 2 from condition U is shown. The shapes of stress/strain curves for all samples are virtually identical except for the value for elongation at failure. Location 2 shows elongation at failure variation from 7% to almost 13%. This level of variance in the measured ductility was typical of all of the samples tested for a given location and processing condition.

Box plots of the condition I tensile property results are shown in Figure 14a,b,c. Location 4 is not noted in the data for condition I because all of the samples failed outside the gage length. If the results from condition I are compared to the results of

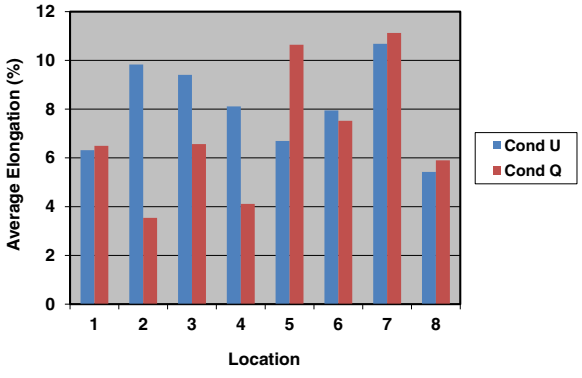

Figure 11 Comparison of average elongation-at-failure (%) behavior in different locations between conditions U and Q.

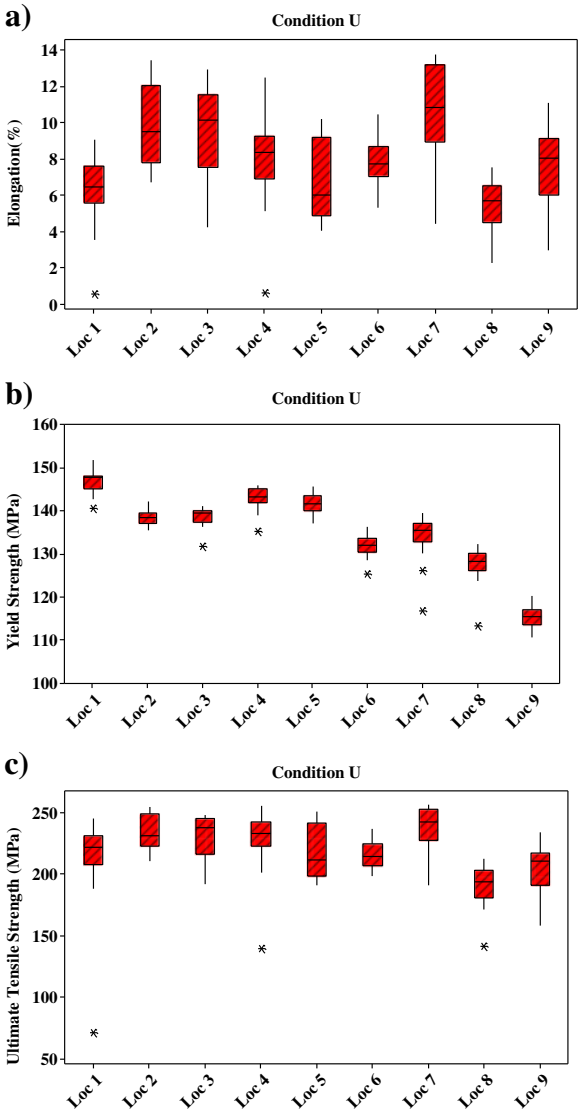

Figure 12 Box plots of tensile results. (a) Elongation at failure (%), **(b)** 0.2% offset yield strength, and **(c)** ultimate tensile strength versus location for tensile samples from condition U. Location numbers correspond to Figure 5. Middle horizontal lines represent median values, upper and lower edges of red boxes represent upper and lower quartile values, and vertical lines extend to minimum and maximum values in data set. Stars (*) signify outlier values.

condition U (Table 4), it can be seen that the elongation at failure is different for several locations, most notably location 2. Location 2 in condition U has an average elongation at failure of 10%, while in condition I, the same location fails at an average elongation at failure of 4%.

Component-level testing

Component-level testing was conducted on two different configurations: a pole test and an axial crush test of the lower part of the GFC casting. All experiments were conducted on a high-speed test frame at the Ford Safety Test Labs in Dearborn, MI, USA.

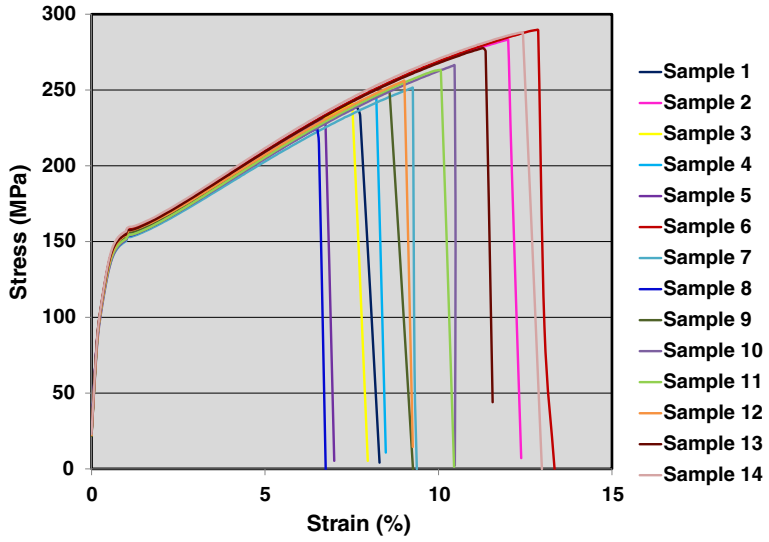

Figure 13 Typical true stress–strain curves for location 2 in condition U.

To run the tests, fixtures were designed to hold the parts stationary while a striker pole was activated to strike the sample at a particular location. The striker pole was loaded to provide a specified force throughout the test. The parts were tested to fracture, and the load and displacement data were recorded as a function of time.

A schematic diagram of the testing configuration for the pole test is shown in Figure 15. The side rails were specifically designed not to constrain the part during deformation. Knife edges were placed in the side rails to hold the part in place prior to the testing. Tape was used to secure the GFC panel to the testing fixture. The round striker pole was 10 cm in diameter. The pole was attached to a sled and then struck the GFC at 3 m/s speeds. The total load impacting the GFCs was 126 kg. A set of approximately 13 tests were performed to determine statistical variability in the testing for condition U. A set of 10 tests were also run for condition I.

Figures 16 and 17 show the force versus displacement curves for conditions U and I, respectively. In both cases, the data from multiple component tests show very consistent behavior. Although the initial peak load is similar for both conditions, the load drops immediately with only 15 to 20 mm of displacement in condition I. Condition U, however, does not experience appreciable load drop until approximately 40 mm of displacement. This leads to considerably less energy absorption for the condition I castings than the condition U. This behavior can be related to the tensile property results (Table 4). Locations 2, 5, and 9 were directly in the path of the striker pole in the pole test. When the values for local ductility are compared for condition U versus condition I, it is observed that condition U had a considerably higher average elongation at failure in location 2 and slightly higher in location 9, which presumably contributed to the better energy absorption under component loading.

Figure 18 shows a comparison of the castings post-test. The condition U casting remains intact, although there are large tears in the middle and lower wall sections and outer wall of the upper aperture is completely fractured through. The condition I casting is broken completely into two pieces.

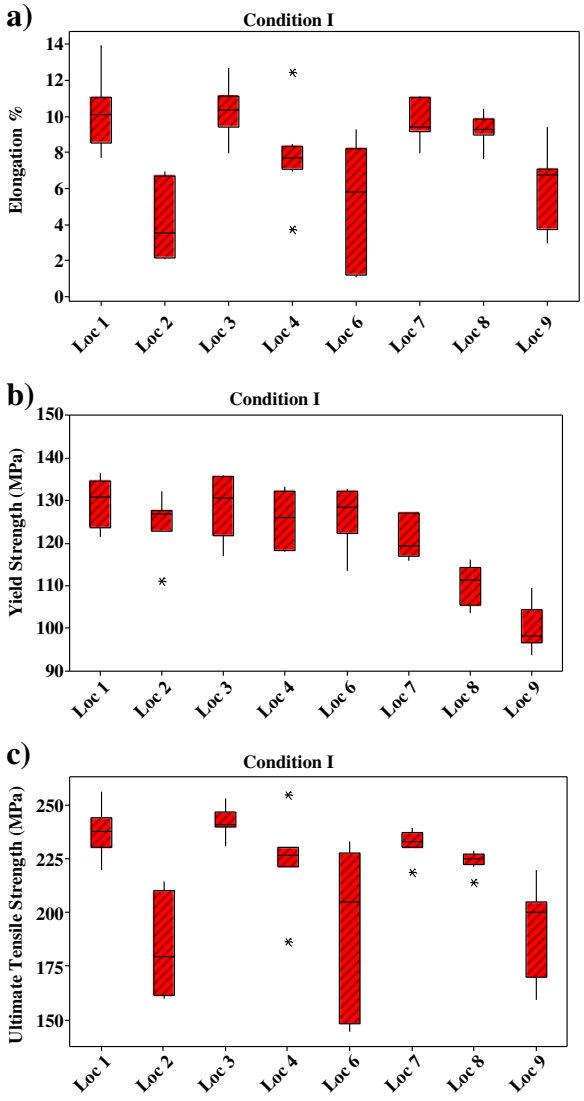

Figure 14 Box plots of tensile property results. (a) Elongation at failure (%), **(b)** 0.2% offset yield strength, and **(c)** ultimate tensile strength versus location for tensile samples for condition I. All samples from location 4 failed outside the gage section and thus were omitted. Location numbers correspond to Figure 5. Middle horizontal lines represent median values, upper and lower edges of red boxes represent upper and lower quartile values, and vertical lines extend to minimum and maximum values in data set. Stars (*) signify outlier values.

For the axial crush testing, only condition U was tested. The GFCs were machined into two sections; the upper window was separated from the lower set of windows, and only the lower window section was tested in axial crush loading. Figure 19 shows a schematic diagram of the testing setup. The casting was placed in a holder with a snug but not clamped fit. The holder contained a draft angle to allow for the casting to be

Table 4 Comparison of uniform elongation in excised samples in conditions U and I

	Average uniform elongation at failure (%)		
	Location 2	**Location 5**	**Location 9**
Condition U	9.8 ± 2.0	6.7 ± 2.2	7.5 ± 2.3
Condition I	4.3 ± 0.8	7.8 ± 0.8	6.0 ± 0.8

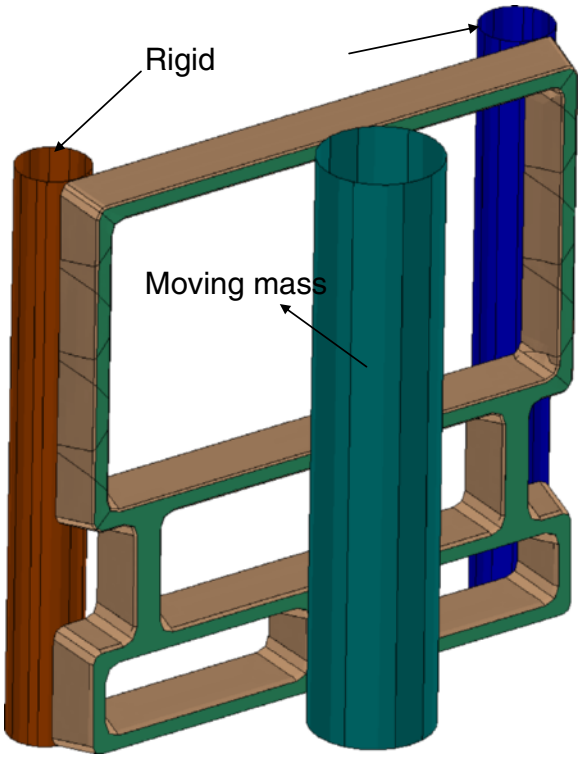

Figure 15 Schematic of the pole test setup for high-speed component-level tests.

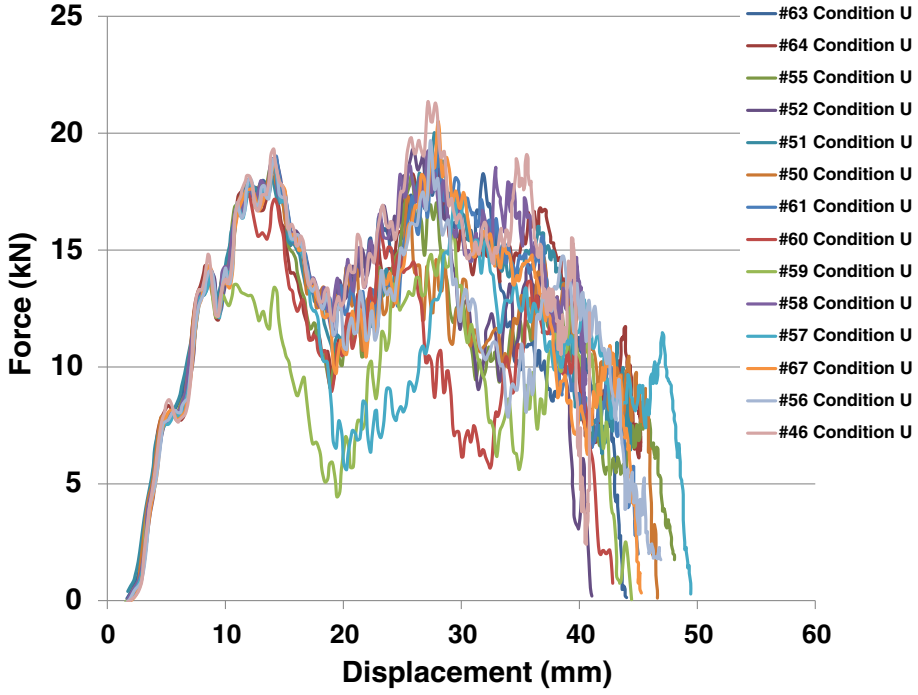

Figure 16 Force versus displacement results for GFC high-speed pole testing of condition U.

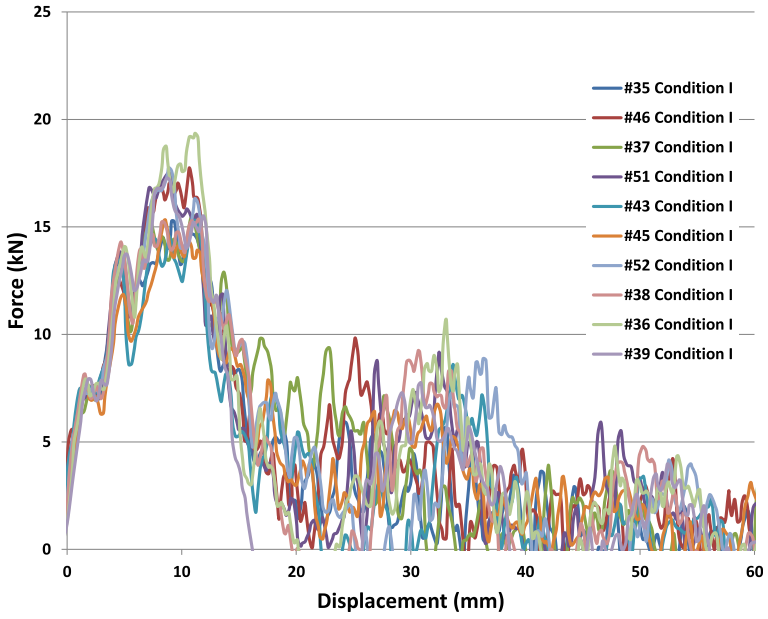

Figure 17 Force versus displacement for GFC high-speed pole testing of condition I.

held in the frame such that the top edge of the casting was parallel to the crosshead. Four tests were conducted on a Bendix™ machine with a speed of 3 m/s. A striker bar was again used to impact the sample, similar to the pole test although the carriage weight in this case was 94 kg. The striker bar impacted the entire surface of the sample, providing a uniform force.

The force versus displacement results are shown in Figure 20. The four tests are very consistent in their behavior, and generally, a peak load of 18 to 20 kN is observed. Only limited cracking was observed in the axial crush tests. Figure 21 shows a typical part after the test. The figure shows that the part deformed in an asymmetrical manner. The column on the left side of the photo indicates more deformation than on the right. This is consistent with the variation in ductility noted in condition U in this location.

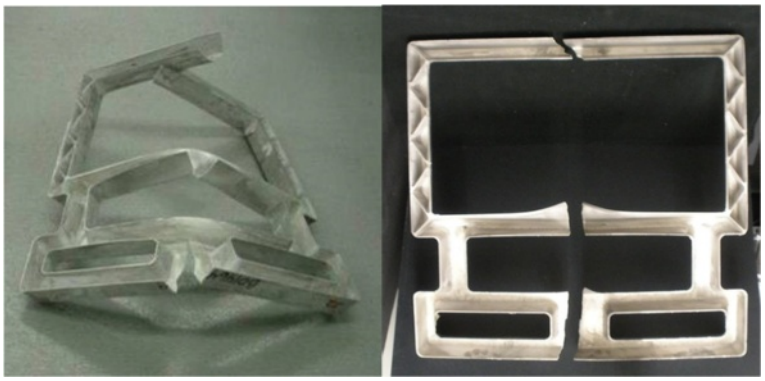

Figure 18 Condition U (left) and condition I (right) castings after testing at 3 m/s. Note higher levels of deformation in condition U.

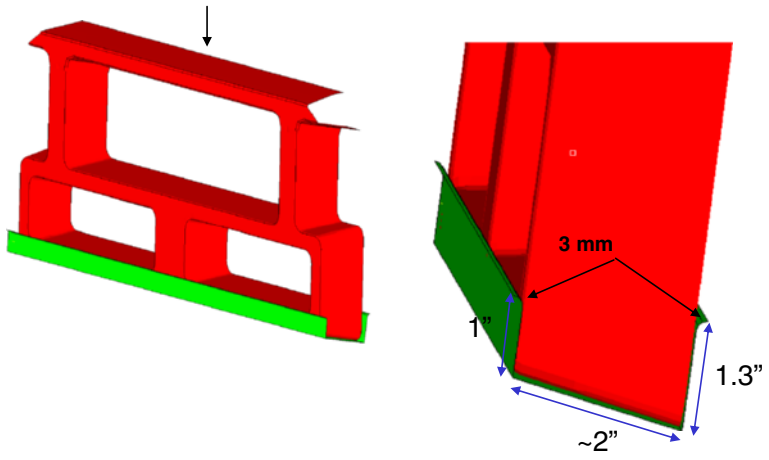

Figure 19 Schematic diagram of axial crush test setup. The part was not clamped but held in the holder with a snug fit. Only the lower portion of the GFC was tested. The upper window was machined away prior to testing.

Derivation of the quality mapping equations

For this study, the quality mapping equation uses several criteria functions identified by the MAGMASOFT® casting simulation code to map the local elongation-at-failure and yield strength predictions onto the cast component geometry. The equation takes the following form:

$$\text{Quality Index} = C_1 * {CF_1}^{C_2} + C_3 * {CF_2}^{C_4} + C_5 * {CF_3}^{C6}$$

where CF is a criteria function that is predicted through the MAGMASOFT® simulation and C_i is a set of constants. MAGMASOFT® has several criteria functions that numerically describe different behaviors in each meshed cell. The criteria functions are based either on flow calculations or on solidification calculations [56].

The criteria functions that were investigated were flow length (FL), solidification time (ST), air contact (AC), temperature at 100% fill (T100%FILL), and air entrapment (AE)

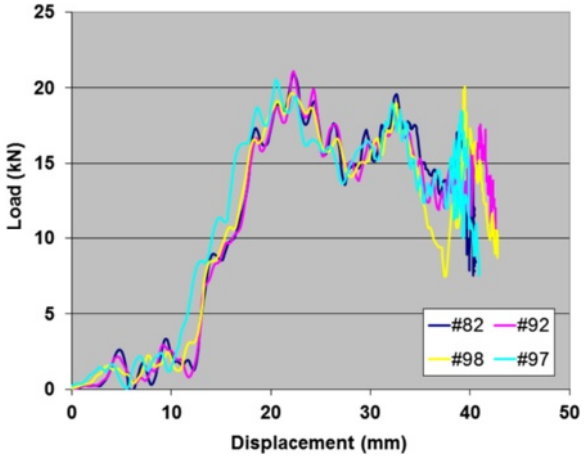

Figure 20 Force versus displacement results for GFC high-speed axial crush testing of condition U (tested at 3 m/s).

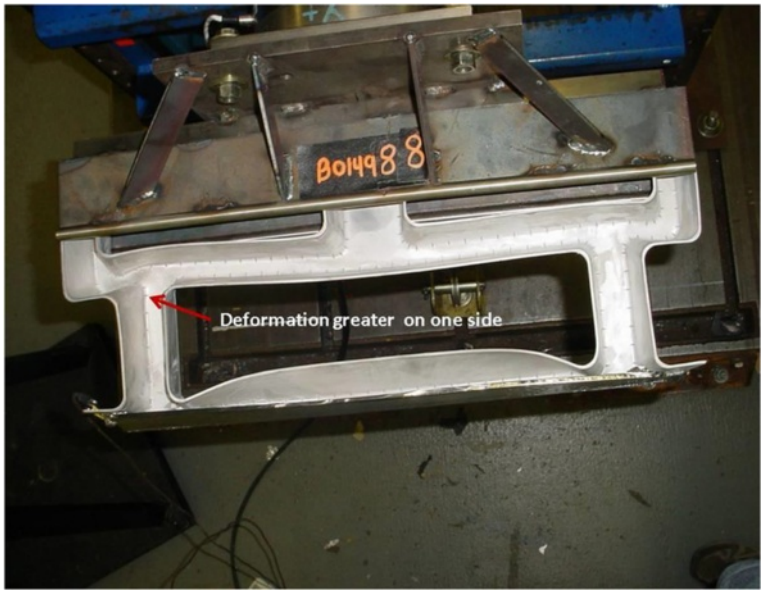

Figure 21 Picture of tested condition U sample indicating asymmetrical deformation.

based on the authors' previous experience and some earlier work from other researchers [4,6,13,14]. Flow length is the length a virtual marker travels in the die cavity before it solidifies. A typical flow length for a frame casting such as a door, instrument panel, or seat could be up to 2 m long depending on gating and overflow positions. Also, if there is significant turbulence, a particle could have a long and tortuous flow length even though the part itself is not large. Solidification time indicates the amount of time required for the temperature in a region to drop from the liquidus to the solidus. Generally, thicker areas will have longer solidification times than thinner areas. Air contact is a proxy for melt front. It gives the amount of time a metal particle is in contact with the air during the casting process. Areas where melt fronts come together tend to have higher times for air contact. Air entrapment estimates the amount of entrapped gas, and temperature at 100% fill indicates the temperature of the melt once filling is complete and the solidification calculations begin. A map of the criteria functions can be observed in the postprocessor, and there is the option to map user results, as well. This output is referred to a USER_Result in the postprocessor. A subroutine and a user input deck were developed to include the empirical equation into the mapping software. This was enabled by using the MAGMASOFT_API code available for version 4.4 of the software.

Separate simulations were conducted using the processing parameters of all of the casting conditions listed in Table 3. In order to have a realistic starting approximation of the mold cavity temperature during casting, the standard practice is to use a simulation procedure in which four 'warm-up' thermal-only simulations were performed first and then the temperature values from the fourth simulation were used as the starting temperature conditions for the flow simulation of the high-pressure die casting process. A total cycle time 45 s was used for the simulation. This allowed for the shot, opening of the die, removal of the part, and then closing of the die. Oil lines were also included in the simulation and were set to a temperature of 190°C in the cover half of the die

and 260°C in the ejector half. These factors were chosen based on the actual casting trial conditions. The MAGMASOFT® HEATMED setting was used for thermophysical properties of the oil, and the interfacial heat transfer settings and the oil lines remained active the entire simulation. The oil lines also remained active during the actual HPDC process of this component.

MAGMASOFT® settings for thermophysical properties and interfacial heat transfer coefficients (IHTCs) of the tool steel for the die were also used (MAGMASOFT® X40CrMoV5 designation). The parameters for the tool steel were temperature dependent. The temperature-dependent IHTCs for each alloy with the tool steel were generated from an internal study. The thermophysical parameters chosen for the Mg alloys were derived from Thermocalc® calculations based on the actual compositions of the alloy used. Temperature-dependent values for heat capacity, thermal conductivity, latent heat, and solidus to liquidus temperature curve were calculated for the AM60 alloy.

The MAGMASOFT® solver uses a finite volume approach. To optimize run time, different parts of the mesh utilized different maximum cell sizes. The casting, gating, and overflows contained cells approximately 0.8 mm × 0.8 mm × 0.8 mm. The ingates to the casting were meshed slightly finer in the flow direction with a cell size of 0.8 mm × 0.5 mm × 0.8 mm to ensure at least three cells across the flow area. Other parts of the casting simulation such as the mold were given a much coarser cell size of 5 mm × 5 mm × 5 mm. Even so, the total number of cells for the simulations was approximately 59 million. Each simulation for the GFC castings required approximately 4 days to complete on a workstation with a single processor. Once each simulation was completed, the results were analyzed and several criteria functions were manually collected in addition to temperature and flow information at the center of each excised tensile sample location. Figure 22 shows an example for the air entrapment output. The color shadings indicate different values for each criteria function in different locations in the casting. The locations of the excised samples and values for the average elongation at failure are indicated as well. In most cases, there was little or no gradient in the criteria functions for a given area so manual selection of the criteria function value in a specific location was straightforward. However, in cases where there was a large change in value for a given criteria function in a particular location, the highest (or in the case of the temperature criteria function, the lowest) value in the center of the wall within a 25-mm area in length was chosen. It was assumed that a sample would fail in the weakest region so a criteria function that could contribute to the weakness would be assumed to be the most extreme value in the region.

The values of several of the criteria functions had quite different orders of magnitude. For example, typical flow length values are between 30 and 200 cm for this study, while most of the values for air contact were less than 0.02. This necessitated the use of normalization factors in the casting. Each criteria function was divided by a value specific to the criteria function. The maximum values for the GFC casting were used in most cases. ST was normalized to 4 s (the maximum solidification time in this casting), air contact was normalized to 0.01 s, and air entrapment was normalized to 0.30. In the case of flow length, the longest distance from the middle of the gate to the overflow on the upper window was used. In this case, it was 90 cm for the GFC. The temperature at 100% fill was normalized to the liquidus temperature of AM60 or 620°C. The

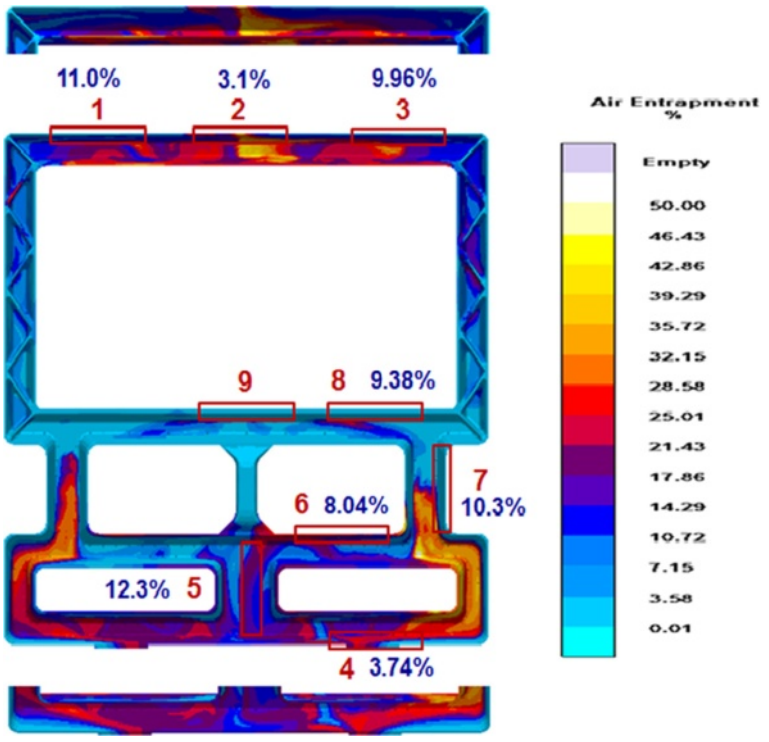

Figure 22 Example of simulation results for air entrapment for condition D and comparison to ductility measurements in each location. The figure indicates the methodology of manual determination of the criteria functions for each location.

assumption in this case is that the higher the value over the liquidus temperature, the less chance that areas would be 'mushy' and feeding or flow would be a problem.

Finally, an initial 'base' elongation at failure of 9% was assumed for the ductility prediction equation. This was an average value of strain at failure associated with an area of the AM60 casting that is considered a desirable or standard target ductility for this alloy. In the case of the yield stress equation, the base value for yield stress for AM60 was considered to be 140 MPa. The regression analysis was performed by comparing the criteria functions generated at each location with the average measured value of the elongation at failure and the yield strength at that location.

The data collected from the simulations (Table 5) was analyzed using the program SigmaPlot®. A linear regression analysis using a least squares fit was performed to obtain the values for each of the eight coefficients in the following equation:

$$\begin{aligned}\text{Strain} = 9 + C_1 * \text{FLnorm}^{C_2} + C_3 * \text{AEnorm}^{C_4} + C_5 * \text{STnorm} +^{C_6} \\ + C_7 * \text{T100\%FILLnorm}^{C_7}\end{aligned}$$

Where

$$\begin{aligned}\text{FLnorm} &= \text{FL}/90 \\ \text{AEnorm} &= \text{AE}/30 \\ \text{STnorm} &= \text{ST}/2.5 \\ \text{T100\%FILLnorm} &= \frac{\text{T100\%FILL} - 620}{620}\end{aligned}$$

Table 5 Locations and their average values for 0.2% offset yield strength and elongation-to-failure with their corresponding criteria functions

Location	Number of samples	Average 0.2% offset yield strength (MPa)	Average elongation (%)	Solidification time (s)	Flow length (cm)	Air entrapment (%)	Temperature at 100% fill
G - 1	18	143 ± 3	8.8 ± 1.8	1.5	90	4	714
G - 4	17	140 ± 2	2.4 ± 1.1	1.64	141	15	697
G - 5	9	146 ± 4	9.5 ± 3.6	1.8	77	12	714
G - 6	14	136 ± 6	4.5 ± 2.3	1.6	84	19	698
G - 7	13	146 ± 7	8.2 ± 2.0	1.64	58	0	706
G - 8	15	137 ± 3	6.4 ± 2.1	1.6	30	19	726
Q - 1	15	143 ± 1	6.5 ± 1.1	1.53	92	4	710
Q - 4	18	143 ± 2	4.1 ± 1.2	1.7	115	15	703
Q - 5	6	146 ± 1	10.8 ± 5.1	1.9	78	12	706
Q - 6	18	120 ± 12	7.5 ± 1.6	1.5	62	15	703
Q - 7	13	141 ± 2	11.1 ± 1.7	1.6	58	17	710
Q - 8	16	130 ± 4	5.9 ± 1.7	1.6	43	19	717
M - 1	14	145 ± 2	9.3 ± 1.6	1.43	94	6.	661
M - 4	11	142 ± 2	4.8 ± 3.5	1.38	106	13	653
M - 5	10	146 ± 2	10.4 ± 3.7	1.64	72	10	661
M - 6	17	141 ± 2	9.2 ± 1.8	1.47	72	13	653
M - 7	18	140 ± 2	8.5 ± 1.3	1.38	60	2	661
M - 8	13	137 ± 2	6.5 ± 1.7	1.47	29	27	669
A - 1	19	140 ± 2	11.5 ± 2.5	1.3	89	6	657
A - 2	16	125 ± 10	3.1 ± 1.4	1.6	112	18	650
A - 3	10	141 ± 2	10.0 ± 1.8	1.3	94	6	657
A - 4	11	139 ± 2	3.7 ± 2.5	1.5	100	19	647
A - 5	16	144 ± 3	12.3 ± 3.2	1.6	80	13	652
A - 6	15	136 ± 3	8.0 ± 1.6	1.4	63	19	655
A - 7	16	134 ± 2	10.3 ± 1.8	1.4	45	0	667
A - 8	15	118 ± 2	9.4 ± 1.3	1.6	31	0	672
J - 1	18	144 ± 2	10.6 ± 1.1	1.43	90	8.	673
J - 2	17	135 ± 2	5.5 ± 1.4	1.54	110	23	667
J - 3	16	146 ± 1	10.2 ± 1.8	1.43	95	12	673
J - 4	10	143 ± 3	9.1 ± 3.3	1.53	80	8	670
J - 5	16	136 ± 3	9.4 ± 2.2	1.8	70	2	670
J - 6	9	138 ± 2	7.9 ± 2.6	1.6	60	10	673
J - 7	17	127 ± 3	12.6 ± 1.6	1.54	45	0	682
J - 8	17	117 ± 2	10.4 ± 2.3	1.7	30	0	688
K - 1	15	142 ± 2	11.5 ± 1.2	1.48	92	8	690
K - 2	19	136 ± 2	4.3 ± 1.6	1.7	130	23	678
K - 3	16	145 ± 2	10.2 ± 2.0	1.48	98	12	690
K - 4	10	143 ± 2	7.8 ± 4.1	1.7	88	8	681
K - 5	12	137 ± 4	12.7 ± 2.6	1.857	55	2	690
K - 6	8	138 ± 2	9.4 ± 3.4	1.59	66	10	693
K - 7	20	130 ± 3	11.0 ± 1.3	1.64	49	0	702
K - 8	15	120 ± 3	10.2 ± 1.4	1.857	33	0	708
D - 1	12	144 ± 2	8.0 ± 2.0	1.5	91.4	4	712
D - 2	16	142 ± 2	7.2 ± 1.6	1.7	109	27	697
D - 3	19	144 ± 2	10.1 ± 1.4	1.5	91.4	8	708

Table 5 Locations and their average values for 0.2% offset yield strength and elongation-to-failure with their corresponding criteria functions *(Continued)*

D - 4	11	142 ± 3	6.3 ± 2.4	1.7	90	11	705
D - 5	18	134 ± 2	9.7 ± 1.5	1.8	85	15	708
D - 6	12	131 ± 11	5.3 ± 3.4	1.6	80	17	708
D - 7	16	117 ± 3	12.5 ± 1.3	1.6	45.7	0	722
D - 8	13	113 ± 1	8.7 ± 2.2	1.9	32.7	0	726

The coefficients for the ductility equation are listed in Table 6. The fit for the prediction equation was $R^2 = 0.60$. Figure 23 shows the measured average strain values and their standard deviations versus the predicted values for all of the data used in the linear regression analysis. The low value of 0.6 for the correlation coefficient is indicative of the many statistical factors that influence ductility that are not captured perfectly in the quality map approach. Despite this low R^2 value, the relationship did provide directional guidance on relative values of high and low ductility values within the castings examined and could still provide some guidance on design (e.g., identify areas of potential weakness). As Figure 23 also shows, this regression is conservative, which was an important consideration for component performance.

A quality map equation for the local yield strength was also determined using a similar procedure. In the case of the yield strength, the differences between the locations were not very significant. There was really only one location that was markedly different in yield strength from the other locations: location 8. This was presumably because this location was closest to the ingate and the solidification time was longer in that region. Therefore, only locations 1 and 8 were used for the linear regression. The average of the yield strength was used for the linear regression. The following equation was developed:

$$\text{Yield stress} = 140 + C_1 * \text{STnorm}^{C_2} + C_3 * \text{FLnorm}^{C_4} + C_5 * \text{T100\%FILLnorm}^{C_6}$$

Where

$$\text{STnorm} = \text{ST}/2.5$$
$$\text{FLnorm} = \text{FL}/90$$
$$\text{T100\%FILLnorm} = \frac{\text{T100\%FILL} - 620}{620}$$

Table 6 Coefficients for the empirical ductility quality map equation developed for MAGMASOFT® version 4.2

	Criteria function	Value
C1	FLnorm	−0.29
C2	Flnorm	4.51
C3	AEnorm	−7.03
C4	AEnorm	0.65
C5	STnorm	−8.06
C6	STnorm	1.95
C7	T100%Fillnorm	4.83
C8	T100%Fillnorm	0.097

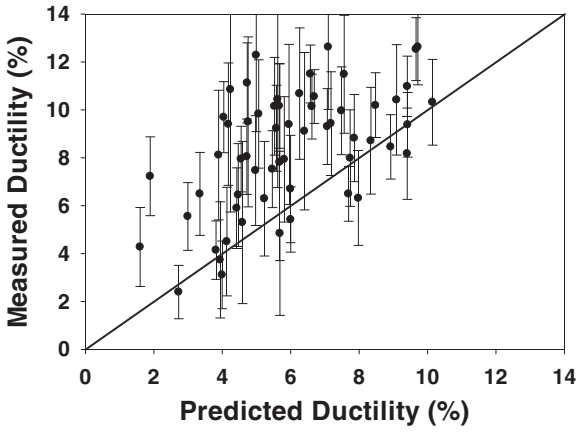

Figure 23 Measured elongation at failure (%) at all locations in all castings versus predicted elongation at failure. The ductility quality map equation for AM60 ($R^2 = 0.6$) was used. Center points represent average elongation, and error bars represent standard deviation for each location and processing condition.

The coefficients are listed in Table 7. Figure 24 shows the measured average yield strength and standard deviation for the various locations produced under different casting conditions versus the estimated yield strength using the quality map equation for yield strength. The fit for the yield strength equation produced $R^2 = 0.84$.

After the equations were developed, they were used as MAGMASOFT® input as user results to map the prediction throughout the casting. They were graphically displayed in the same manner as other results were presented in the program and provided a map of the local property of interest.

The quality mapping equations were developed using the results from tests conducted under the partial factorial DOE. Next, the quality mapping procedure and equations were used to examine local property differences between conditions U and I. First, the differences in the criteria functions as a function of location were compared for the two casting conditions. Additional files 2 and 3 show an animation comparison of the flow of melt in front and back views in the two castings, illustrating the differences in pattern between the two conditions. Figures 25, 26, and 27 indicate the local differences in air entrapment, flow length, and temperature at 100% fill, respectively.

Figure 28 shows the predicted elongation at failure as mapped onto condition U and condition I. The comparison indicates that the ductility prediction captures the

Table 7 Coefficients for the empirical yield strength quality map equation developed for MAGMASOFT® version 4.2

	Criteria function	Value
C1	STnorm	−271.33
C2	STnorm	8.84
C3	Flnorm	67.53
C4	Flnorm	0.19
C5	T100%Fillnorm	−47.13
C6	T100%Fillnorm	−0.11

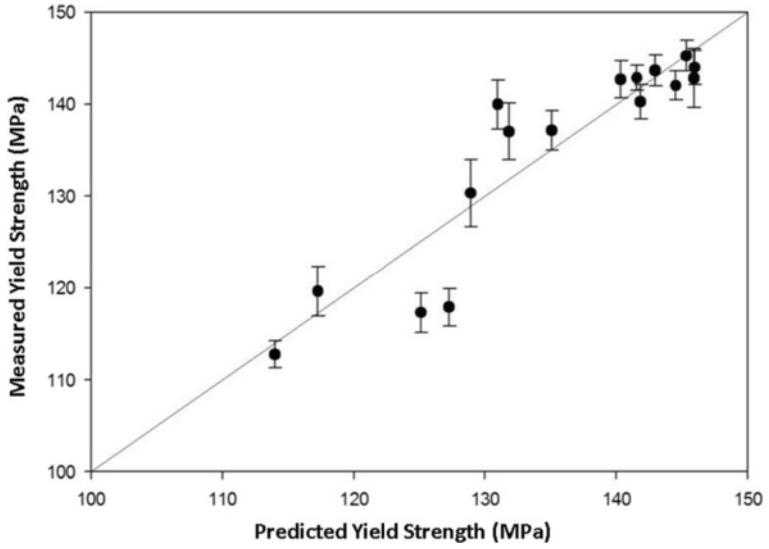

Figure 24 Measured yield strength at locations 1 and 8 for all casting conditions versus predicted yield strength. The yield strength quality map equation for AM60 castings ($R2 = 0.84$) was used.

differences between condition U and condition I at location 2 very well. Other locations show good comparison to the prediction. Figure 29 shows a comparison of the yield strength predictions for condition U and condition I. Both conditions indicate a trend of increasing yield strength with distance from gating, as also seen in the experimental results. However, the difference in yield strength between condition U and condition I is not captured in the prediction.

It must be noted that these equations and coefficients were specifically developed for use in MAGMASOFT® version 4.2. They have not yet been validated with other versions of MAGMASOFT® or other casting simulation codes.

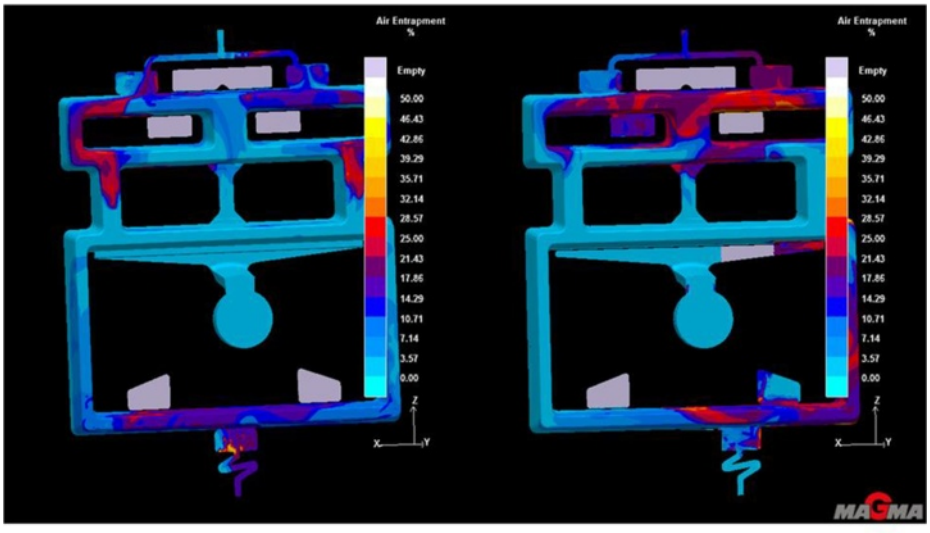

Figure 25 Comparison of air entrapment for condition I and condition U.

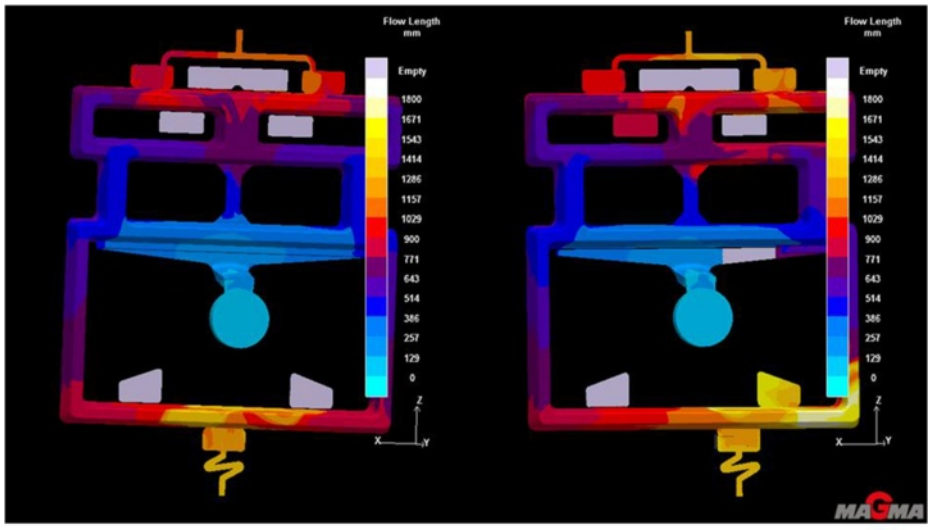

Figure 26 Comparison of flow length for condition I and condition U.

Application of the quality mapping for local properties

The GFC casting was specifically designed to be an experimental cast part substitute for a large thin-walled frame casting. Therefore, in order to test the quality mapping equation for ductility, a prototype liftgate inner casting produced by Meridian Lightweight Technologies (Strathroy, ON, Canada) was analyzed. The casting was produced in AM60 on a 4,200-ton HPDC production machine at a different facility from the GFC production. Figure 30 shows a schematic diagram of the prototype casting examined along with the locations of excised tensile samples. Flat sub-sized tensile bars were excised from 15 locations on the casting with a total of 10 castings machined. Tensile testing was conducted

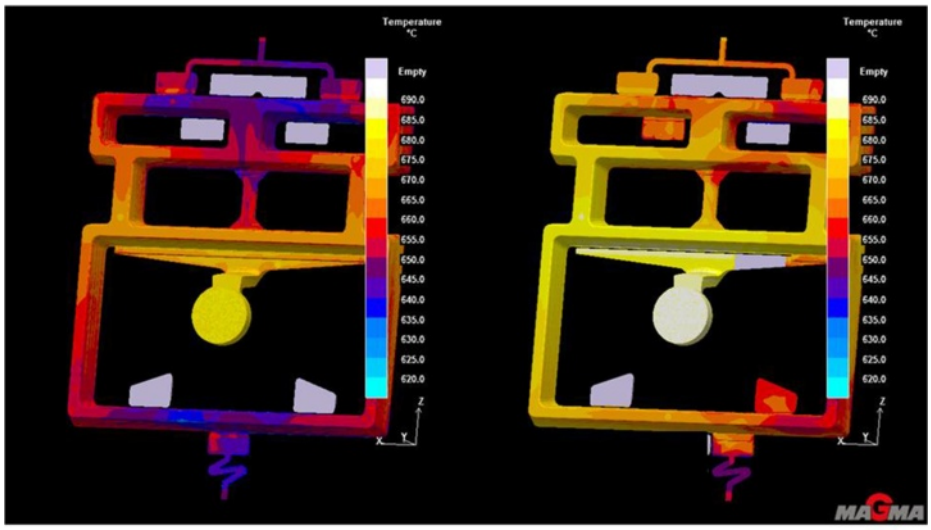

Figure 27 Comparison of temperature at 100% fill for condition I and condition U.

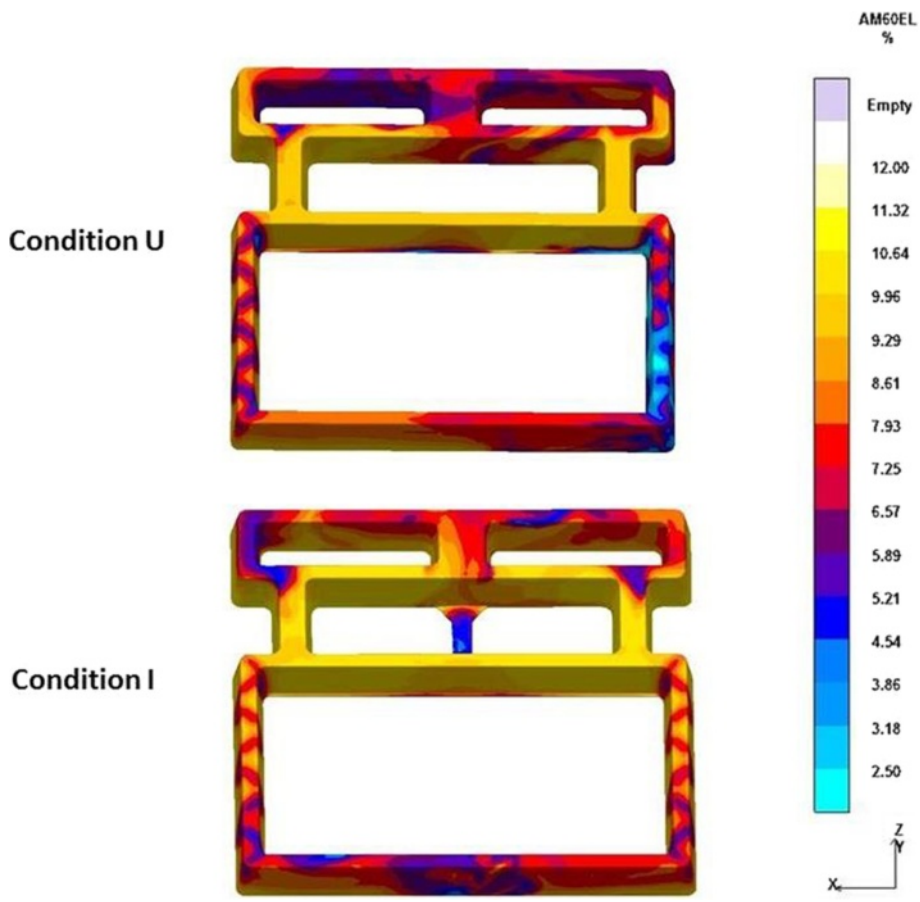

Figure 28 Predicted elongation at failure map of condition U versus condition I.

using a similar procedure and protocol to that previously described for the GFC testing. A complete MAGMASOFT® version 4.2 simulation was performed using the production processing parameters provided by the prototype casting supplier.

The quality mapping equation was then applied using the criteria function outputs from the simulation. The coefficients applied to the postprocessor were the same as those that were generated for the GFC. However, some changes were made to the normalization factors to accommodate the fact that the casting was much larger. Most notably, the flow length criteria function normalization parameter was changed from 90 to 200 cm to represent the longest flow length for that casting.

Figure 31 shows a plot of average measured elongation and standard deviation versus predicted elongation for the prototype casting. The predictions show good agreement for all locations with the exception of locations 6 and 7. In location 6, many of the samples failed at or close to yield. Examination of the fracture surface of many of the samples indicated defects and discolored material in the center of the sample possibly indicative of oxide films. One possible explanation for the failure of the model to predict the poor performance in this area may be due to a condition in this casting that was not present in the GFC. The GFC did explore different gating configurations; however, in both cases a single gate was used. The prototype casting tooling used six separate gates to fill the casting. These multiple gate melt fronts are not quantifiably

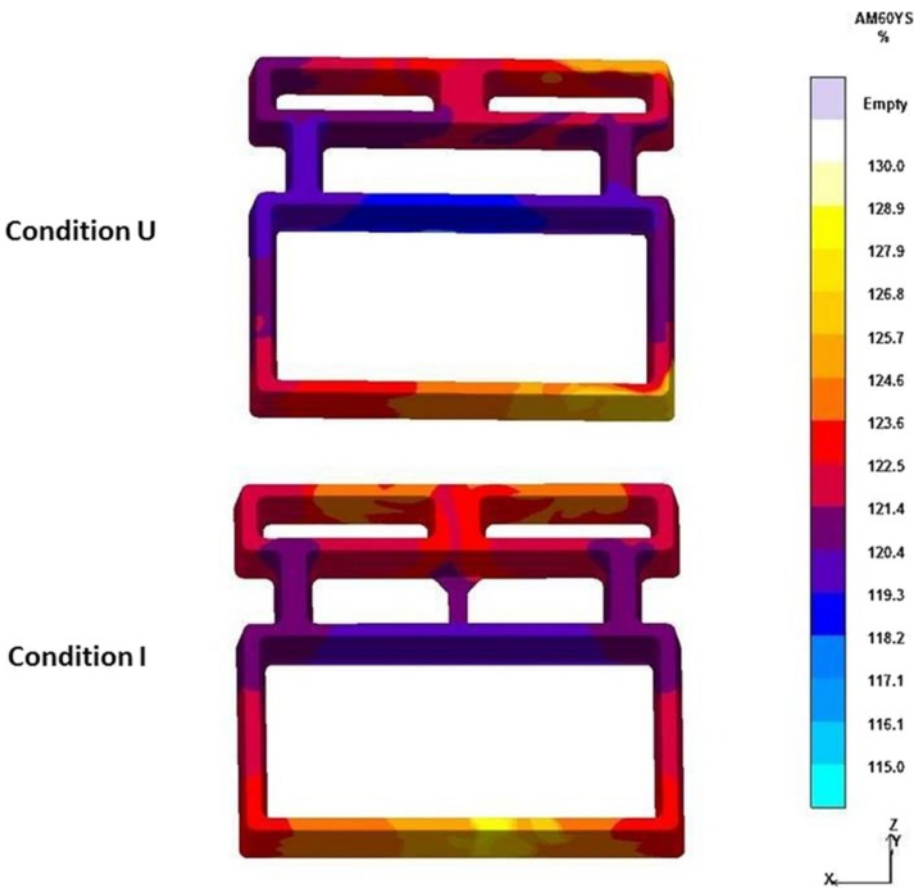

Figure 29 Predicted yield strength map for conditions U and I.

Figure 30 Prototype automotive door inner casting and locations of excised tensile samples.

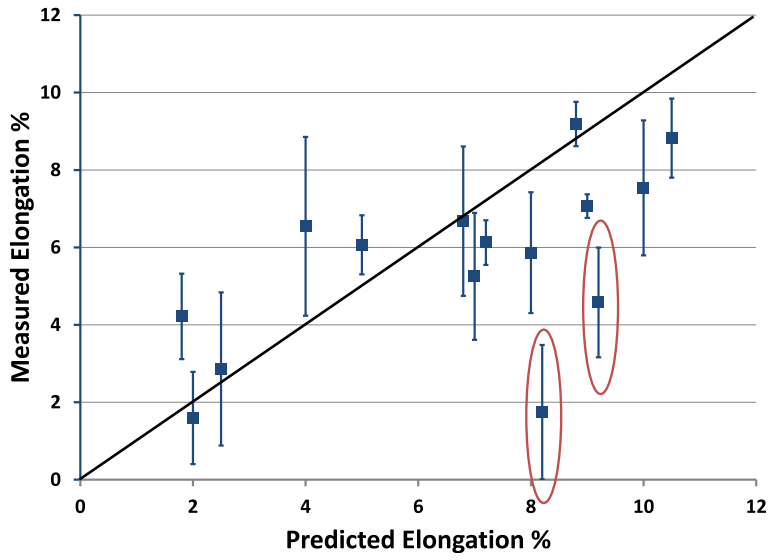

Figure 31 Measured average elongation at failure (%) and standard deviation versus predicted elongation at failure. Agreement was acceptable except for two locations (circled).

described in the casting simulation code. Location 6 is in a region where the different gate melt fronts meet and that may have influenced the behavior in this region. More work is needed to identify an appropriate criteria function to determine these effects, or an index can be assigned based on the program outputs to quantify these interactions. Examination of location 7 indicated no obvious reason for the discrepancy between the model and the prediction. However, the prototype casting exhibited variation of wall thickness across the part from 2.5 up to 5 mm, a condition not present in the areas examined in the GFC. This could have influenced flow conditions in a way that cannot be accounted for in the empirical quality mapping equation.

Utilizing local property predictions for performance predictions

In the ICME methodology, the ultimate use of manufacturing history sensitive local property prediction is in component performance prediction. Establishing the spatial variability in local properties for different casting conditions was important for understanding the overall behavior of the component during component performance prediction and confirmation testing. The predicted elongation-at-failure and yield strength values of a GFC geometry were used in a high-speed component performance simulation to establish the extent to which the component performance could be predicted or influenced by the local properties. In this study, the finite element solver code used was LS_DYNA®. These simulation results were compared to high-speed pole and axial crush testing described earlier.

The LS_DYNA® simulations were conducted using shell elements approximately 5 mm in length. The casting was divided into 17 different sections, and each section was meshed (shown in Figure 32). A base stress/strain curve was provided for the material using an average stress/strain curve from location 2 in condition U (curve from sample 10 in Figure 13). That curve was modified for each section in the GFC mesh based on the quality map-predicted local properties from the casting simulation.

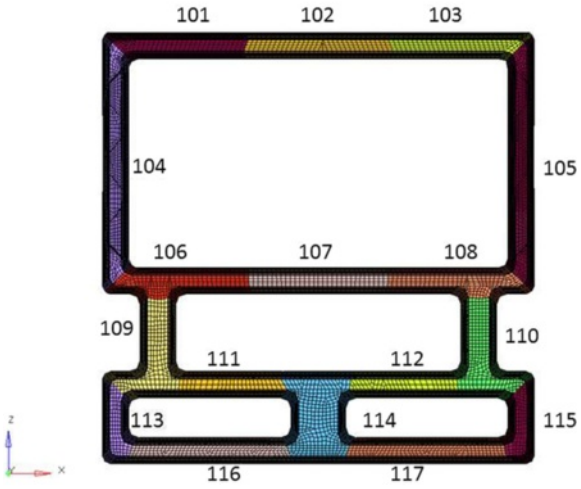

Figure 32 GFC mesh divided into 17 different regions for LS_DYNA simulation. Each region was assigned a different material card based on the MAGMASOFT® simulation.

Tables 8 and 9 show how the curve was modified based on the local property predictions to generate the input data for the material input deck for each meshed section. As indicated in Table 8, the yield strength was only changed in one location on the GFC. This reflected the region immediately adjacent to the gate that had a longer solidification time and a lower measured yield strength than other areas in the casting. The material input deck used in this simulation was MAT_24 (MAT_PIECEWISE_LINEAR_PLASTICITY).

Table 8 Elongation at failure values used for each GFC section in LS_DYNA® pole test and axial crush test simulations

Mat ID	Condition I	Condition U
101	0.08	0.03
102	0.03	0.06
103	0.08	0.11
104	0.08	0.04
105	0.08	0.07
106	0.09	0.10
107	0.05	0.07
108	0.09	0.09
109	0.09	0.06
110	0.09	0.10
111	0.09	0.04
112	0.09	0.10
113	0.08	0.03
114	0.05	0.05
115	0.08	0.10
116	0.06	0.05
117	0.06	0.07

Table 9 Stress factor used to modify the local yield strength prediction for each GFC section

Mat ID	Condition I	Condition U
101	1.0	1.0
102	1.0	1.0
103	1.0	1.0
104	1.0	1.0
105	1.0	1.0
106	1.0	1.0
107	0.875	0.875
108	1.0	1.0
109	1.0	1.0
110	1.0	1.0
111	1.0	1.0
112	1.0	1.0
113	1.0	1.0
114	1.0	1.0
115	1.0	1.0
116	1.0	1.0
117	1.0	1.0

Failure was defined by the total strain at failure in the stress–strain curve defined for all elements in the region. When the failure strain was reached in that element, it was deleted.

Force versus displacement curves were generated from the simulations for both condition I and condition U in the pole test case. Those results are shown in Figure 33. There is good agreement in both cases between the CAE predictions and the actual test results. Animations of the tests are shown in Additional files 4 and 5. The animations indicate the earlier total failure of the condition I GFC when compared to the condition U GFC.

A force versus displacement curve was also generated from the LS_DYNA® simulation for the axial crush testing performed on the condition U sample (see Figure 34). An animation of the behavior during testing indicates buckling on one side of the test (Additional file 6). This indicates that the local properties in that area caused the region to yield and fracture earlier in the deformation than the other side and are an indication of the value of the ICME approach for product development.

Discussion

A comparison of the different casting parameters and their associated tensile properties at various locations indicated that, in the case of the thin-walled frame casting investigated in this study, the flow characteristics dominated the local tensile properties for both experiments and predictions. Changing the casting parameters that impacted the flow conditions either globally or locally within the casting had the most significant effect on the ductility, whereas processing parameters such as melt temperature, which would affect solidification, appeared to play a lesser role. Gating configuration, a

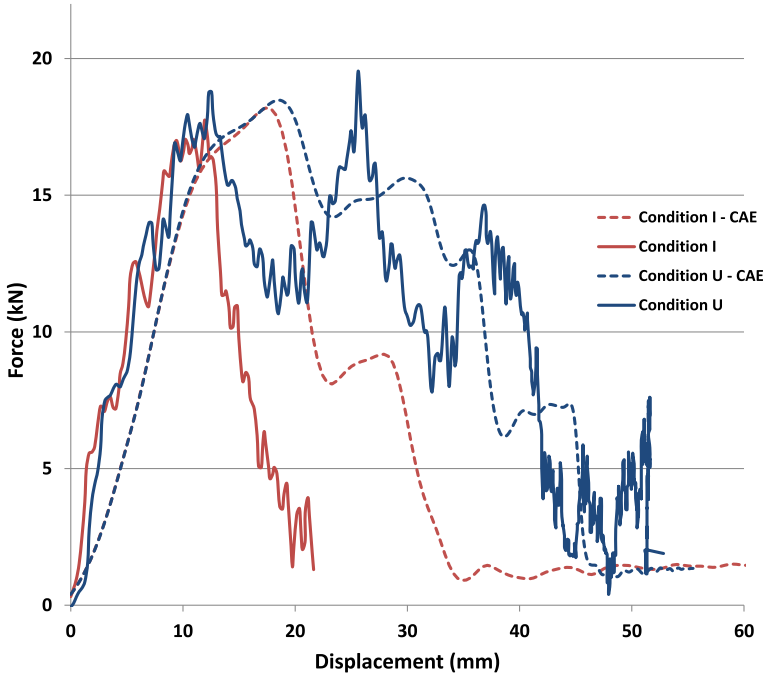

Figure 33 Force versus displacement curves. Comparison of force versus displacement data generated from LS_DYNA® simulations compared with experimental component test results for the 3 m/s pole test.

geometrical parameter, consistently shows a larger influence on the ductility for most of the locations than most of the other casting parameters examined, as can be observed in Figure 9. Figure 11 illustrates the influence of overflow placement on the flow characteristics in a casting. Conditions U and Q are virtually identical except for the placement of the overflows. Those overflows are significant because they capture the melt fronts and remove them from the casting itself. This is evident not only in the

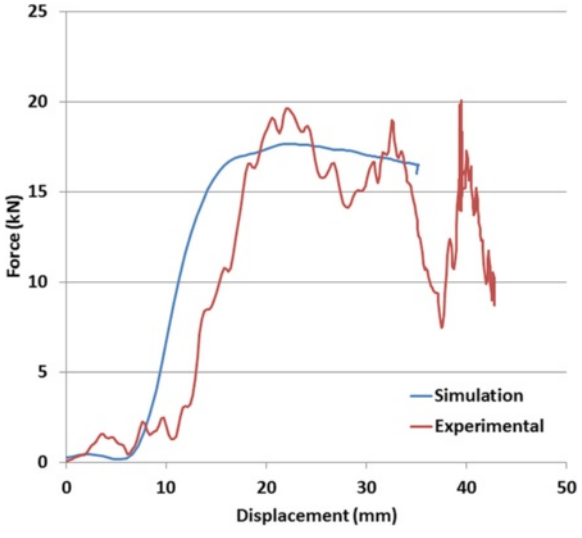

Figure 34 Force versus displacement curves. Comparison of force versus displacement data generated from LS_DYNA simulations compared with experimental component results for the axial crush test (3 m/s).

experimental results, but it is also captured by the quality mapping ductility model (Figure 35). Comparing these two conditions illustrates the importance of melt fronts and melt flow turbulence in the prediction of general ductility in areas of the casting.

As shown in Figure 9, in locations where melt fronts meet (e.g., location 2 and location 5), processing parameters such as melt temperature and shot speed appeared to have some influence over the ductility. A lower initial melt temperature tended to result in a lower ductility for these locations because the lower temperature could result in lower melt feeding into those areas that were last to fill, resulting in more shrinkage-related porosity and a higher likelihood that metal closer to the liquidus temperature would have lower fluidity and less ability for that melt to be pushed out of the casting into the overflows. A high shot speed could either contribute positively to the ductility in a location by pushing poor metal out of the casting quicker (location 2) or negatively by contributing to local turbulence and defect creation (location 5). A faster shot speed, however, was only an improvement in the ductility in the symmetrical gating configuration. In the asymmetrical gating configuration, it actually reduced the ductility in location 2. This could be due to potentially increased turbulence in the region for the asymmetrical gating configuration.

Once the inputs to the casting simulation were understood, the outputs of the casting simulation were also important to evaluate. The criteria functions of flow length, melt

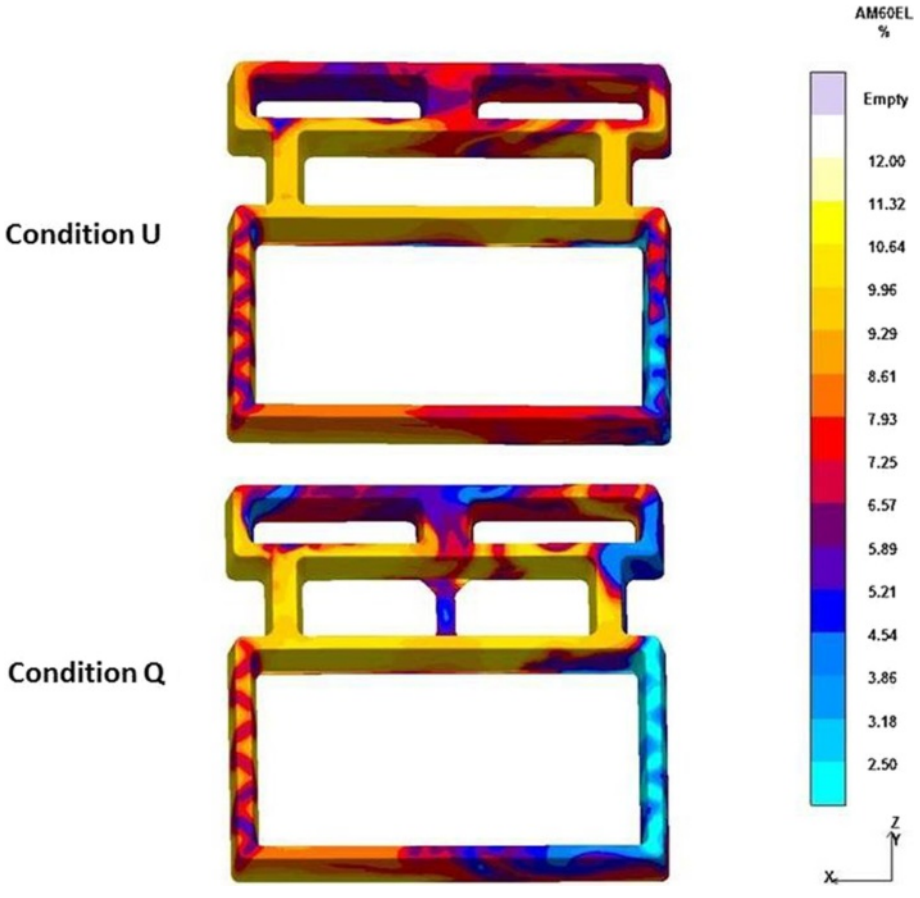

Figure 35 Predicted elongation at failure map of condition U versus condition Q.

temperature at 100% fill, air entrapment, and solidification time were used in the quality mapping procedure in part because they were independently calculated parameters in the MAGMASOFT code that can represent the flow and solidification behavior observed in cast parts. The criteria function, solidification time, is a good indicator of solidification gradients which can have an effect on yield strength. Indeed, the most heavily weighted parameter in the yield strength quality map equation was solidification time, with only minor contributions coming from flow length or temperature at 100% fill. Unfortunately, the effects of melt flow turbulence and melt fronts coming together, key areas that have been shown to have a significant influence over the local ductility in this study, are less well-defined using the criteria functions available. Normalized flow length, air entrapment, and temperature at 100% fill were proxies for the melt flow conditions that could contribute to differences in ductility from the simulation. These criteria functions were used together with similar weighting to describe local ductility. While the use of these particular criteria functions did appear to at least capture trends in the local ductility in the GFC casting, there was some disagreement when the equation was used to predict local ductility in the large prototype casting. This could potentially indicate the need to identify an additional criteria function or functions within the code to capture some additional effects (such as melt flow behavior from multiple gates).

One important issue throughout this work was the need to recognize that uncertainty exists throughout the casting, simulation, mechanical testing, and modeling trials performed. Panchal et al. [57] have highlighted this as a key issue in the practical application of ICME approaches. There will be some variability in the processing parameters from casting to casting in a single trial (e.g., slight changes in shot profile or minor changes in melt temperature). The casting simulation process relies on the accurate input of all casting parameters and thermophysical properties. While the authors attempted to be as accurate as possible and measured all process parameters carefully during each trial, some input parameters, of necessity, were averages or estimates. The starting melt temperature, for example, was averaged across the trial based on the temperature measured in the shot sleeve. A fast shot speed was also estimated from overlays of many individual shot profile curves for each condition. The heat transfer coefficients between a solidifying melt and the die wall can only be estimated based on embedded thermocouples in a die, and while the ones used in this case were temperature dependent, no accommodation was made for whether the casting was freezing onto the mold wall or freezing away. Fluidity is also an estimated value based on limited measurements of similar alloys.

The experimental results of the excised samples indicated a great deal of statistical variability particularly in the ductility measurements. This made it difficult to determine a single value of the mechanical property to use in the regression analysis for the modeling (in this case, the authors simply used the average). It was not clear if there was inherent variability in the sample or if the variation seen was, in part, caused by the excising of the test bar from the cast part. Alain et al. [58] proposed that the variability observed in tensile tests was due to the removal of the as-cast surface during machining of the sample and much of the resulting scatter in the results was due to the exposure of internal porosity or other defects due to the machining. Weiler et al. [13,14] and Yang et al. [59-61] have reported the pronounced decreases in mechanical

properties in Mg alloys between areas closest to the surface ('skin') and areas in the middle of the cross section ('core'). Therefore, the act of excising and testing a tensile sample from a component could indicate more mechanical property variation, particularly in elongation at failure, than actually exists in the cast component. Indeed, though there was significant statistical variability in the excised sample testing for a given location, the force versus displacement behavior of the overall component in the loading situations examined in this study was repeatable within a very tight range. The average peak load for the component-level high-speed pole testing for condition U was 17.8 kN with a standard deviation of 1.3 kN, and the average peak load for the condition I component-level testing was 16.6 kN with a standard deviation of 1.5 kN. The load versus displacement curves also indicated consistent displacement values for final failure (40 mm for condition U and 20 mm for condition I).

The quality mapping process also produced some uncertainty. Selection of the criteria functions relied on a manual analysis of each region of interest in each of the eight simulations. While, most of the time, the region of interest contained a single value of a particular criteria function, there were some instances where a judgment was made because of large gradients in the outputs. Further, a simple linear regression analysis was used to develop the model. The authors recognize that other techniques exist to produce a correlation that could potentially more accurately predict the mechanical properties of interest.

It is also important to point out that this case study involved transferring one prediction from one simulation code into another simulation code to perform another prediction. One of the issues with doing this is the change in scale of the mesh itself. In the casting simulation code, the cell size of the mesh must be small to accurately predict the flow of the melt, and the mesh size in this study was typical of what would be used in an actual component casting simulation. However, a component performance simulation would utilize a much larger mesh size. This poses an issue when trying to transfer a local ductility prediction to material input deck of a code such as LS_DYNA. The authors tried to avoid this issue by manually dividing the casting into regions of interest and then determining a low value for each region based on the quality mapping output from the casting simulation. This introduces some uncertainty in the selection of mechanical properties for a given location but allows for simplification of the performance simulation to address areas of interest in a computationally efficient manner.

Finally, the current investigation deliberately avoided the microstructure prediction to go to a direct processing to property prediction. Measured property values were used to compare to the simulation results, and the quality map approach infers that the microstructural variables that affect properties are captured in the combined and weighted criteria functions. This assumption does not appear to be unreasonable in the case where the casting has a fairly uniform wall thickness (even with a complex shape). However, many automotive castings have large variations in wall thickness. This can result in enough variation in microstructural features (such as skin thickness and microporosity locations or segregation of elemental composition) that those features need to be independently predicted and their impact fundamentally understood. Indeed, the failure of the quality mapping equation to predict the ductility in all of the tested locations in the large prototype frame casting may have also been due to limited ability to predict local microstructure in those regions. Further work is required to improve upon the current state of the art.

Conclusions

- A thin-walled frame high component was produced by high-pressure die casting to investigate the effect of processing conditions on the local and component-level mechanical behavior of AM60.
- A casting DOE was conducted to determine the effects of casting parameters on local ductility. Castings were produced and detailed processing parameters such as die temperature and shot speed were collected.
- Tensile properties, specifically elongation at failure and yield strength, were characterized from a subset of the casting DOE, and the main effects were determined for each location. The effect of geometrical parameters was the most important for all locations, but melt temperature and shot speed were important for certain locations.
- MAGMASOFT® version 4.2 simulations were conducted for all of the conditions from the DOE and two additional conditions (condition U and condition I), and several criteria functions from the local areas corresponding to the excised tensile samples were determined and used in development of an empirical quality map for prediction of local properties.
- The quality mapping equation was utilized in the local property predictions of three separate castings: two frame castings (conditions U and I) and a prototype automotive door inner casting.
- The quality map-predicted local properties were used in an LS_Dyna® model to simulate two different component tests. The LS_Dyna® prediction showed good correlation with experimental component test results.
- Quality mapping represents an important ICME tool for predicting local properties in HPDC Mg components and can provide a good estimate of local property trends for frame-like castings. This methodology can be utilized to incorporate the manufacturing history into casting design upfront and potentially reduce the number of physical prototype iterations required to verify component performance.

Additional files

Additional file 1: A schematic diagram of a typical cold-chamber high-pressure die cast machine.
Additional file 2: Flow comparison of conditions I and U from the front side.
Additional file 3: Flow comparison of conditions I and U from the rear side.
Additional file 4: Animation of condition I pole test.
Additional file 5: Animation of condition U pole test.
Additional file 6: Animation of condition U axial crush test.

Competing interests
The authors declare that they have no competing interests.

Authors' contributions
JF, ML, and JA developed the overall quality mapping approach for Mg components and design of program. JWZ and LG designed GFC casting, developed the casting design of experiment, and conducted all casting trials. JF and JZ conducted all casting simulations, and JF conducted and analyzed all tensile testing and assisted with the design and analysis of component-level trials. JF, ML, and JZ conducted regression analysis and developed quality mapping equations, and JZ conducted simulation sensitivity analyses. JF and ML supervised LS_DYNA® simulations. All authors read and approved the final manuscript.

Acknowledgements
JF would like to acknowledge Sheila Ryzyi of Ford Motor Company for assistance with tensile testing, Ari Caliskan of Ford Motor Company for assistance with the design of the component tests, and the Ford Safety Lab for the high-speed testing. JWZ and LG would like to acknowledge the support of Mag-Tec Casting in Jackson, MI for assistance with the casting trials. We acknowledge helpful discussions with and support of X. Sun, Pacific Northwest National Laboratory (Batelle Memorial Institute). We would also like to acknowledge Meridian Lightweight Technologies, Inc., for assistance with the prototype casting simulation and mechanical testing. JZ and JA wish to acknowledge the financial support of Battelle Memorial Institute and US Department of Energy under Contract No. DE-AC05-76RL01830. Their work was funded by the Department of Energy Vehicle Technologies Office under the Automotive Lightweighting Materials Program managed by William Joost.

Author details
[1]Materials Research Department, Ford Motor Company, Research and Innovation Center, MD3182, P.O Box 2053, Dearborn, MI 48121, USA. [2]Department of Materials Science and Engineering, University of Michigan, 2300 Hayward St., Ann Arbor, MI 48109, USA.

Received: 7 August 2014 Accepted: 2 March 2015
Published online: 02 April 2015

References

1. Friedrich HE, Mordike BL (2006) Magnesium Technology: Metallurgy, Design Data, Application. Springer, Berlin
2. Schumann S (2005) Paths and strategies for increased magnesium applications in vehicles. Mater Sci Forum 488–489:1–8
3. Schumann S, Friedrich H (2003) Current and future use of magnesium in the automobile industry. Mater Sci Forum 419–422:51–56
4. Grebetz JC (1993) A Comparison of the Impact Characteristics of Several Magnesium Die Casting Alloys. SAE Tech. Pap, Ser, 930417
5. Padfield CJ, Padfield TV (2002) Plane stress fracture toughness testing of die cast magnesium alloys. SAE Tech. Pap., Ser. 2002-01-0077
6. Chen X, Wagner DA, Houston DQ, Cooper RP (2004) Elongation variability of AM60 die cast specimens. 2004 ASME International Mechanical Engineering Congress.
7. Coultes BJ, Wood JT, Wang G, Berkmortel R (2003) Mechanical properties and microstructure of magnesium high pressure die castings. In: Kaplan HI (ed) Magnes. Technol. 2003. The Minerals, Metals, and Materials Society, pp 45–50.
8. Weiler JP, Wood JT, Klassen RJ, Maire E, Berkmortel R, Wang G (2005) Relationship between internal porosity and fracture strength of die-cast magnesium AM60B alloy. Mater Sci Eng A A395:315–322
9. Wood JT, Klassen RJ, Gharghouri MA, Maire E, Wang G, Berkmortel R (2005) Mechanical properties of AM60B die castings: a review of the AUTO21 program on magnesium die-casting. SAE Tech. Pap., Ser. SAE-2005-0725
10. Carlson BE (1995) The effect of strain rate and temperature on the deformation of die cast AM60B. SAE Tech. Pap., Ser. SAE-950425
11. Li M, Zindel J, Godlewski L, Allison J (2006) Prediction of porosity defects and mechanical properties of high pressure die cast A380 aluminum alloy components. TMS Lett 3:31–32
12. Horstemeyer MF, Wang P (2003) Cradle-to-grave simulation-based design incorporating multiscale microstructure-property modeling: reinvigorating design with. J Comput Mater Des 10:13–34
13. Weiler JP, Wood JT, Basu I (2012) Process-structure–property relationships for magnesium alloys. Mater Sci Forum 706–709:1273–1278, doi:10.4028/www.scientific.net/MSF. 706–709.1273
14. Weiler JP, Wood JT, Klassen RJ, Berkmortel R, Wang G (2006) Variability of skin thickness in an AM60B magnesium alloy die-casting. Mater Sci Eng A 419:297–305, doi:10.1016/j.msea.2006.01.034
15. Laukli HI, Lohne O, Arnberg L (2005) High Pressure Die Casting of Aluminum and Magnesium Alloys - some comparisons of Microstructure Formation. Shape Cast. John Campbell Symp, TMS Annual Meeting
16. Dahle AK, Lee YC, Nave MD, Scha PL, StJohn DH (2001) Development of the as-cast microstructure in magnesium-aluminum alloys. J Light Met 1:61–72
17. Rodrigo D, Murray M, Mao H Brevick J, Mobley C, Chandrasekar V, Esdaile R (1999) Effects of section size and microstructural features on the mechanical properties of die cast AZ91D and AM60B magnesium alloy test bars. SAE Tech. Pap., Ser. 1999-01-0927
18. Rodrigo D, Murray M, Mao H, Brevick J, Mobley C, Esdaile R (1999) Characteristic microstructural features of die cast magnesium alloys. World Die Cast. 20th Int. Die Cast. Congr. Expo. NADCA, pp 219–225.
19. Rodrigo D, Ahuja V (2000) Effect of casting parameters on the formation "pore/segregation" bands in magnesium die castings. In: Aghion E, Eliezer D (eds) Magnes. 2000 Proc. 2nd Isr. Conf. Magnes. Sci. Technol. Magnesium Research Institute Ltd, Dead Sea, Israel, pp 97–104
20. Mao H, Brevick J, Mobley C Chandrasekar V, Rodrigo D, Murray M (1999) Microstructural characteristics of die cast AZ91D and AM60 magnesium alloys. SAE Tech. Pap., Ser. 1999-01-0928
21. Chadha G, Allison JE, Jones JW (2007) The role of microstructure on ductility of die-cast AM50 and AM60 magnesium alloys. Metall Mater Trans A 38A:286–296
22. Dahle AK, StJohn DH (1999) Rheological behavior of the mushy zone and its effect on the formation of casting defects during solidification. Acta Mater 47:31–41
23. Dahle AK, StJohn DH (1999) The origin of banded defects in high pressure die cast magnesium alloys. World Die Cast T99–062:205–211
24. Bowles AL, Griffiths JR, Davidson CJ (2001) Ductility and the skin effect in high pressure die cast Mg-Al alloys. In: Hryn J (ed) Magnes. Technol. 2001. The Metals Mineral and Materials Society, pp 161–168
25. Dahle AK, Sannes S, St. John DH, Westengen H (2001) Formation of defect bands in high pressure die cast magnesium alloys. Journal of Light Metals 1:99–103
26. Sannes S, Gjestland H, Westengen H, Laukli HI, Lohne O (2003) Die casting of magnesium alloys - the importance of controlling die filling and solidification. SAE Tech Pap., Ser SAE–2003–01–0183

27. Wang G, Froese B, Bakke P (2003) Process and property relationships in AM60B die castings. Magensium Technol. 2003 The Metals Mineral and Materials Society.
28. Cao H, Wessen M (2004) Effect of microstructure on mechanical properties of As-Cast Mg-Al alloys. Metall Mater Trans A 35A:309–319
29. Cao H, Wessen M (2005) Characteristics of microstructure and banded defects in die cast AM50 magnesium components. Int J Cast Met Res 18:377–384
30. Cao H, Wessen M (2003) Modeling of microstructure - mechanical property relations in cast Mg-Al alloys. In: D. M. Stefanescu, Warren J, Jolly M, Krane M (eds) Model. Cast. Welding, Adv. Solidif. Process. X. The Minerals, Metals, and Materials Society, pp 165–172.
31. Forsmark JH, Boileau J, Houston D, Cooper R (2012) A microstructural and mechanical property study of an AM50 HPDC magnesium alloy. Int J Met 6:15–26
32. Lee CD, Shin K (2007) Effect of microporosity on the tensile properties of AZ91 magnesium alloy. Acta Mater 55:4293–4303, doi:10.1016/j.actamat.2007.03.026
33. Lee CD (2007) Tensile properties of high-pressure die-cast AM60 and AZ91 magnesium alloys on microporosity variation. J Mater Sci 42:10032–10039, doi:10.1007/s10853-007-2003-1
34. Choi KS, Li D, Sun X, Li M, Allison J (2013) Effects of pore distributions on ductility of thin-walled high pressure die-cast magnesium. SAE Tech Pap, Ser. doi:10.4271/2013-01-0644
35. Unigovski Ya, Tuman E, Eliezer A, Riber L, Koren Z (2000) Correlation of mechanical properties of die cast magnesium alloys with processing conditions. In: Aghion E, Eliezer D (eds) Magnes. 2000 Proc. 2nd Isr. Int. Conf. Magnes. Sci. Technol. Magnesium Research Institute, Dead Sea, Israel, pp 105–111
36. Gjestland H, Sannes S, Svalestuen J, Westengen H (2005) Optimizing the magnesium die casting process to achieve reliability in automotive applications. SAE Tech. Pap., Ser. SAE 2005–0333
37. Gertsberg G, Nagar N, Lautzhe M Bronfin B, Moscovitch N, Schumann S (2005) Effect of HPDC parameters on the performance of creep resistant alloys MRI153M and MRI230D. SAE Tech. Publ., SAE 2005–0
38. Greve L (2004) Development of a PAM-CRASH material model for die casting alloys. Magnes. Proc. 6th Int. Conf
39. Sannes S, Gjestland H, Westengen H, (2005) The use of quality mapping to predict performance of thin-walled magnesium die casting. SAE Tech Pap. Ser. 2005-01-0332.
40. Dorum C, Hopperstad OS, Langseth M, Lademo OG (2005) Numerical modeling of the structural behavior of thin-walled cast magnesium components using a through-process approach. SAE Tech. Pap., Ser. 2005-01-07
41. Dorum C, Hopperstad OS, Landemo O-G, Langseth M (2005) Numerical modelling of the structural behavior of thin-walled cast magnesium components. Int J Solids Struct 42:2129–2144
42. Dorum C, Hopperstad OS, Lademo O-G, Langseth M (2006) An experimental study on the energy absorption capacity of thin-walled castings. Int J Impact Eng 32:702–724
43. Dorum C, Hopperstad OS, Lademo O-G, Langseth M (2007) Energy absorption capacity for thin-walled AM60 castings using the shear-bolt principle. Comput Struct 85:89–101
44. Dorum C, Hopperstad OS, Berstad T, Dispinar D (2009) Numerical modelling of magnesium die-castings using stochastic fracture parameters. Eng Fract Mech 76:2232–2248
45. Weiss U, Bach A (2011) Magnesium HPDC Crash CAE. La Met Ital 103(11–12):1–9
46. Li N, Osborne R, Cox B, Penrod D (2005) Magnesium Engine Cradle - The USCAR Structural Cast Magnesium Development Project. SAE Trans., 2005-01-03
47. Balzer JS, Dellock PK, Maj MH, Cole GS, Reed D, Davis T, Lawson T, Simonds G (2003) Structural magnesium front end support. SAE Tech. Pap., Ser. 2003-01-0186
48. Blanchard PJ, Bretz GT, Subramanian S, deVries JE, Syvret A, MacDonald A, Jolley P (2005) The application of magnesium die casting to vehicle closures. SAE Tech. Pap., Ser. 2005-01-0338
49. Gibbs S (2010) Magnesium structural part parts with myth. Met Cast Des Purch 12:29–33
50. Herman EA (1996) Gating and Die Casting Dies, E-514th ed. NADCA Publications, Rosemont, IL, USA
51. North American Die Casting Association (1998) Magnesium Die Castings Handbook, #201 ed. NADCA Publications, Rosemont, IL, USA
52. Box GEP, Hunter WG, Hunter JS (1978) Statistics for Experimenters. John Wiley & Sons, New York
53. ASTM E8/E8M - 13a (2015) Standard test methods for tension testing of metallic materials 1., pp 1–28, doi: 10.1520/E0008
54. Khan S (2012) Box-and-whisker plots. In: Khan Acad., https://www.khanacademy.org/math/probability/descriptive-statistics/box-and-whisker-plots/v/reading-box-and-whisker-plots
55. Minitab 15 statistical software statguide (2012), Minitab Inc., State College, PA USA
56. MAGMASOFT version 4.4 user manual, MAGMA Foundry Technologies Inc., Aachen, Germany.
57. Panchal JH, Kalidindi SR, McDowell DL (2013) Key computational modeling issues in Integrated Computational Materials Engineering. Comput Des 45:4–25, doi:10.1016/j.cad.2012.06.006
58. Alain R, Lawson T, Katool P, Wang G, Jekl J, Berkmortel R, Miller L, Svalestuen J, Westengen H (2004) Robustness of large thin wall magnesium die castings for crash applications. Reprinted from: Magnesium for automotive components. SAE Tech Pap., Ser 2004–01–0131
59. Yang KV, Cáceres CH, Easton MA (2013) A microplasticity-based definition of the skin in HPDC Mg–Al alloys. Mater Sci Eng A 580:355–361, doi:10.1016/j.msea.2013.05.018
60. Yang KV, Easton MA, Cáceres CH (2013) The development of the skin in HPDC Mg–Al alloys. Mater Sci Eng A 580:191–195, doi:10.1016/j.msea.2013.05.017
61. Yang KV, Cáceres CH, Easton MA (2014) Strengthening micromechanisms in cold-chamber high-pressure die-cast Mg-Al alloys. Metall Mater Trans A 45:4117–4128, doi:10.1007/s11661-014-2326-x